Evolution of the glacial landscape of the Southern Alps of New Zealand : Insights from a glacial erosion model

Frédéric Herman, Jean Braun

Evolution of the glacial landscape of the Southern Alps of New Zealand: Insights from a glacial erosion model

Frédéric Herman[1,2,3] and Jean Braun[4]

Received 3 April 2007; revised 30 September 2007; accepted 23 November 2007; published 3 May 2008.

[1] A new version of a landscape evolution model that includes the evolution of an ice cap at a 10^3 to 10^5 year timescale and its associated erosion patterns is presented and applied to the Southern Alps of New Zealand. Modeling of the ice cap evolution is performed on a higher-resolution grid (i.e., ~100 m) than previously (Braun et al., 1998). It predicts which parts of the landscape are, and have been, affected by glacial erosion. The model results highlight the complexity of the erosion patterns induced by ice caps and glaciers. Glacial erosion in a tectonically active area is, as suggested by the model, not uniform across the mountain range. Furthermore, high rock uplift rates, heavy precipitation, and climatic oscillations constantly interact. The feedback mechanisms are such that they render the landform very dynamic and transient. However, under conditions of reduced rock uplift rate and precipitation, the landform becomes more stable at the timescale of the glacial cycle. Finally, the modeling results favor a tectonic model in the Southern Alps in which the maximum rock uplift is offset from the Alpine Fault.

Citation: Herman, F., and J. Braun (2008), Evolution of the glacial landscape of the Southern Alps of New Zealand: Insights from a glacial erosion model, *J. Geophys. Res.*, *113*, F02009, doi:10.1029/2007JF000807.

1. Introduction

[2] Active research on the evolution of mountain landforms has focused on the issue of climatic versus tectonic forcing [e.g., *Raymo and Ruddiman*, 1992; *Molnar and England*, 1990; *Reiners et al.*, 2003; *Burbank et al.*, 2003] and the understanding of the dominant processes responsible for the evolution of the topography and its relief [e.g., *Brozovic et al.*, 1997; *Whipple et al.*, 1999]. However, most geodynamical models employed have focused on fluvial and hillslope erosion [e.g., *Koons*, 1990; *Beaumont et al.*, 1992; *Avouac and Burov*, 1996; *Willett*, 1999; *Willett et al.*, 2001] and have neglected the effects of glacial erosion. While stream power laws are commonly used for fluvial erosion, the role of ice caps and glaciers in shaping the topography is still a matter of animated discussions [e.g., *Adams*, 1980; *Whitehouse*, 1987; *Brozovic et al.*, 1997; *Whipple et al.*, 1999; *Tomkin*, 2000; *Brocklehurst and Whipple*, 2002; *Shuster et al.*, 2005; *Herman and Braun*, 2006b; *Herman et al.*, 2007].

[3] Several authors have postulated mechanisms that explain the evolution of glacial landscapes. For instance, glaciated landscapes shaped by warm-based glaciers have been described as being smooth, with a decrease of mean slope at elevations above and around snow lines independent of the rock uplift rate. This is known as the glacial "buzzsaw" hypothesis [*Brozovic et al.*, 1997]. Alternatively, numerous qualitative or small-scale models have been proposed to explain how the ice may sculpt the landscape [e.g., *Hallet*, 1979; *Boulton*, 1974, 1979; *Harbor*, 1992a, 1992b; *Hallet*, 1996; *MacGregor et al.*, 2000; *Alley et al.*, 2003; *Fabel et al.*, 2004; *Anderson et al.*, 2006; *Koppes and Hallet*, 2006]. These often include the importance of widening of valleys, formation of U-shaped valleys, overdeepenings of longitudinal profiles, development of towering hillslopes, cirque expansions. On the contrary, few studies have successfully quantified the long-term (thousands to millions of years) and mountain range scale spatial patterns of denudation rates [e.g., *Braun et al.*, 1998; *Tomkin and Braun*, 2002; *Spotila et al.*, 2004; *Kessler et al.*, 2006; *Ehlers et al.*, 2006; *Densmore et al.*, 2007]. The purpose of this study is to assess the spatial and temporal role of glacial erosion at the scale of an orogen and at a 10^3 to 10^5 year timescale. This is achieved by developing a large-scale glacial erosion model similar to [*Braun et al.*, 1998] but which has the advantage of simulating glacial erosion at a higher spatial resolution. We first present the physical assumptions behind the model as well as the adopted modeling approach. We then test its applicability to the case of the Southern Alps of New Zealand. While the role of fluvial erosion during the postglacial period in the Southern Alps of New Zealand has been addressed in an earlier paper [*Herman and Braun*,

[1]Research School of Earth Sciences, Australian National University, Canberra, ACT, Australia.
[2]Geological and Planetary Science Division, California Institute of Technology, Pasadena, California, USA.
[3]Geologisches Institut, ETH Zurich, Zurich, Switzerland.
[4]Géosciences Rennes, Université de Rennes 1, Rennes, France.

0148-0227/08/2007JF000807

2006b], here we focus on another key aspect in the geomorphic evolution of this active mountain belt that requires better understanding: the spatial and temporal role of glacial erosion. We first address this issue herein by simulating the evolution of an ice cap on the present-day landscape in response to climate changes without including any erosion or tectonic forcing. We then describe a series of experiments which include the effects of erosion and tectonics and finally discuss their consequences in the context of the Southern Alps.

2. Ice, Erosion, and Tectonic Models

[4] In this section, we present the numerical model and its underlying assumptions. Our approach is similar to that of *Braun et al.* [1998]. The model requires the computation of the geometry of an ice cap to determine the ice velocity at the ice-bedrock interface. Mass and force balance are used under the so-called "thin ice" approximation to compute the regions of ice accumulation and ablation and estimate the extent, thickness and velocities of the ice. Once the ice thickness and velocities are calculated, the glacial erosion rates can be estimated. In regions that are not covered by the ice, we compute erosion rates by fluvial and hillslope processes.

2.1. Ice Model

[5] The ice thickness, h (m), is determined by solving the equation of mass conservation of the ice:

$$\frac{\partial h}{\partial t} = \nabla \mathbf{q} + M \tag{1}$$

where $\mathbf{q}$ is the vertically averaged mass flux ($\mathbf{q} = h\mathbf{u}$, where $\mathbf{u}$ is the vertically integrated horizontal ice velocity (m a^{-1}) and M the mass balance (m a^{-1})).

[6] The ice velocity, $\mathbf{u}$, consists of two terms: the deformation velocity ($\mathbf{u_d}$) and the sliding velocity ($\mathbf{u_s}$). The so-called shallow ice approximation (SIA) is used [*Hutter*, 1983] to compute these velocities with great efficiency:

$$\mathbf{u_d} = \frac{2B}{p+2}(\rho g)^p h^{p+1} |\nabla(h+z)|^{p-1} \nabla(h+z) \tag{2}$$

$$\mathbf{u_s} = \frac{B_s}{N-P}(\rho g)^p h^p |\nabla(h+z)|^{p-1} \nabla(h+z) \tag{3}$$

where B is the ice flow law parameter (m^6 a^{-1} N^{-3}), B_s the sliding law parameter (m^7 a^{-1} N^{-3}), ρ the density of the ice (kg m^{-3}), g the gravitational acceleration (m^2 a^{-1}), p Glen's flow parameter, N the ice overburden pressure (N m^{-2}), P the water pressure (N m^{-2}) and z (m) the bedrock topography. $\mathbf{u_s}$ is only calculated where the temperature of the ice at the bedrock-ice interface is at melting point (see below for the treatment of the temperature within the ice).

[7] By substituting equation (2) and (3) into (1), one obtains:

$$\frac{\partial h}{\partial t} = \nabla\left(\frac{2B}{p+2}(\rho g)^p h^{p+2} + \frac{B_s}{N-P}(\rho g)^p h^{p+1}\right) \cdot |\nabla(h+z)|^{p-1}\nabla(h+z) + M \tag{4}$$

which is solved using a fully explicit finite difference scheme, following *Hindmarsh and Payne* [1996]. In addition, the effect of the constriction [*Svennson*, 1958] of the ice flow into narrow valleys is implemented by computing a constriction factor, β, which is used to scale the velocities:

$$\beta = \left(1 + k_c \frac{\partial^2 z}{\partial x_c^2}\right)^{-1} \tag{5}$$

where k_c (m) is a constant and x_c indicates the direction normal to the direction of ice flow.

[8] One last important assumption is that the complex flow of water underneath the ice is not addressed here [e.g., *Kessler and Anderson*, 2004]. To keep the model sufficiently simple to model the long-term evolution of glaciated landscapes (which requires many times steps of relatively short duration, i.e., a few years), N-P is taken equal to $0.8N$ following *Knap et al.* [1996] and *Braun et al.* [1998].

[9] Dirichlet boundary conditions are used for the thickness of the ice. Here h is set to nil for the models presented herein.

2.2. Altitudinal Mass Balance

[10] The altitudinal mass balance, M, is the net amount of snow or ice accumulated or ablated over a year at different altitudes. The equilibrium line altitude (ELA) corresponds to the regions (altitudes) on the landscape where M is nil (locally ablation is perfectly compensated by accumulation). M is regarded as the sum of two terms: M_s, the surface mass balance (m a^{-1}) and M_m the melting rate at the base (m a^{-1}).

[11] M_s is assumed to be directly proportional to the surface temperature:

$$M_s = -\gamma_1 (T_s - 0.5) \tag{6}$$

where γ_1 is an arbitrary constant, $T_s = T_0$-$\alpha(h+z)$-0.7576λ, with T_s being the surface temperature, T_0 the mean sea level temperature at the equator, α the atmospheric lapse rate(°C m^{-1}) or rate of change of temperature with altitude in the atmosphere, and λ the latitude.

[12] We have tested different methods to estimate the rate of melting at the base. We concluded that it is more accurate to adopt the method described by *Braun et al.* [1998], rather than estimating a melting rate that is simply proportional to the geothermal gradient and the frictional heat induced by sliding [*Paterson*, 1994]. In the adopted method, the temperature of the ice at the ice-bedrock interface (T_b) is first estimated. At each time step, this calculation depends on the value of M that has been computed at the previous step. In the accumulation area, where M is positive, the vertical advection of heat is taken into account and

$$T_b = T_s + \frac{G}{K}\frac{\sqrt{\pi}}{2}\sqrt{\frac{2h\kappa}{M}} erf\left(h\sqrt{\frac{M}{2h\kappa}}\right) \tag{7}$$

where K is the thermal conductivity of the ice (W m^{-1} K^{-1}), κ is the thermal diffusivity (m^2 a^{-1}), and G is the basal geothermal gradient (W m^{-2}). In the ablation area, where M is negative, a linear thermal gradient is assumed within the ice layer. In regions where the ice temperature at

the base of the ice sheet is at or above melting point T_m, we compute M_m according to:

$$M_m = -\gamma_2(T_b - T_m) \tag{8}$$

where γ_2 is an arbitrary constant. We take into account the dependence of the ice melting temperature on pressure by estimating T_m from: $T_m = -8.7 \times 10^{-4}$ [*Hooke*, 1998].

[13] Parameters γ_1 and γ_2 are regarded as free parameters which we select to produce a reasonable mass balance,i.e., one that reproduces the observed positions of the ELA in the present climatic conditions and at the Last Glacial Maximum (LGM) in the study area. Although it may be regarded as an oversimplification, this approach insures that we successfully reproduce a reasonable altitude-mass balance relationship which is often regarded as the primary control on the geometry and thus dynamical behavior of the ice cap [*Paterson*, 1994]. It also reduces the degree of complexity of the model rather than introducing parameters that are poorly constrained such as the frictional heat produced at the base of the ice or the exact rate of accumulation/melting as a function of ice temperature.

2.3. Erosion Model

2.3.1. Glacial Erosion

[14] Erosion by glaciers includes a combination of several mechanisms such as chemical weathering, subglacial stream erosion, abrasion by entrained rocks and/or plucking of bedrock [e.g., *Lliboutry*, 1994]. These mechanisms and their interactions are complicated and several theories have been advanced [e.g., *Andrews*, 1972; *Boulton*, 1974, 1979; *Hallet*, 1979, 1996; *Lliboutry*, 1994; *Alley et al.*, 2003]. Here we follow the same approach as *Braun et al.* [1998] and *Tomkin* [2000] where the glacial erosion is simply taken to be a function of the ice-sliding velocity u_s at the ice-bedrock interface [*Hallet*, 1979]:

$$\frac{\partial z}{\partial t} = K_g |u_s|^l \tag{9}$$

where K_g ($m^{1-l}\ a^{l-1}$) is the glacial erosion constant and l an arbitrary exponent. Following *Tomkin and Braun* [2002] and *Harbor* [1992a, 1992b] l is chosen equal to 1.

2.3.2. Fluvial Erosion

[15] In regions that are not covered by the ice, we impose that fluvial erosion and hillslope processes are actively eroding the landscape. To parameterize fluvial incision, we adopt a "classical" power law [e.g., *Howard*, 1994; *Whipple and Tucker*, 1999]:

$$\frac{\partial z}{\partial t} = K_f A^m (\nabla z)^n \tag{10}$$

where K_f ($m^{(1-2m)}\ a^{-1}$) is the erosion constant, A (m^2) the drainage area, weighted by spatial variations in the precipitation rate, and ∇z the local slope; m is taken equal to 1/2 and n to 1. Incision only occurs where there is no ice.

[16] In regions of high elevation, precipitation may be locally controlled by orography, i.e., decompression-induced condensation of the water content of a mass of air forced to rise over surface topography. To prescribe the topographic control on precipitation we adopt the method described by *Beaumont et al.* [1992], where the precipitation is a function of the altitude and the distance, x (m), traveled by the moist air across the mountain range in the prevailing wind direction.

$$P(x) = \frac{h + z}{C_1} C_2(x) \tag{11}$$

$$C_2(x) = C_0 - \triangle x \sum_{i=1}^{N} P(i \triangle x) \tag{12}$$

where C_0 (a^{-1}), C_1 (m^2) and C_2 (a^{-1}) are arbitrarily chosen to produce the desired/observed precipitation pattern. P (m a^{-1} m^{-2}) is the assumed precipitation per unit area and Δx is the mesh size. This is then integrated over time and introduced in a "cascade" algorithm to calculate A as described by *Braun and Sambridge* [1997].

2.3.3. Hillslope Erosion

[17] Hillslope erosion mechanisms are largely described in the literature [e.g., *Davis*, 1892; *Gilbert*, 1909; *Koons*, 1987; *Beaumont et al.*, 1992; *Braun and Sambridge*, 1997; *Herman and Braun*, 2006a] and, when integrated over the appropriate (i.e., long) timescales and length scales, are commonly represented by a simple, linear diffusion equation:

$$\frac{\partial z}{\partial t} = D \nabla^2 z \tag{13}$$

where D ($m^2\ a^{-1}$) is a constant. This equation is derived from the principle of mass conservation and the assumption that mass flux is proportional to local slope. It is worth noting that this erosion term is only computed in regions of the landscape where there is no ice, including ice-free peaks or nunataks. In these cases, the diffusion equation is meant to represent periglacial processes rather than landsliding or soil creep on lower elevation, and thus more temperate, ice-free parts of the landscape.

2.4. Tectonic Model

2.4.1. Flexural Isostasy

[18] We assume that the system is in regional, flexural isostatic equilibrium and we approximate this behavior by computing the vertical deflection of an elastic plate subject to vertical loading. The load includes the weight of the ice as well as that of the material added and removed at the surface by surface processes. The differential equation that governs the deflection, w (m), of a thin elastic plate is [*Turcotte and Schubert*, 1982]:

$$F \nabla^4 w = q(x, y) \tag{14}$$

where F is the flexural rigidity (Nm) and $q(x)$ the vertical load (N m^{-2}). F is computed as follows:

$$F = \frac{E h_f^3}{12(1 - \nu^2)} \tag{15}$$

where E is the Young's modulus (Pa) and ν the Poisson coefficient; h_f is the assumed effective elastic thickness (m)

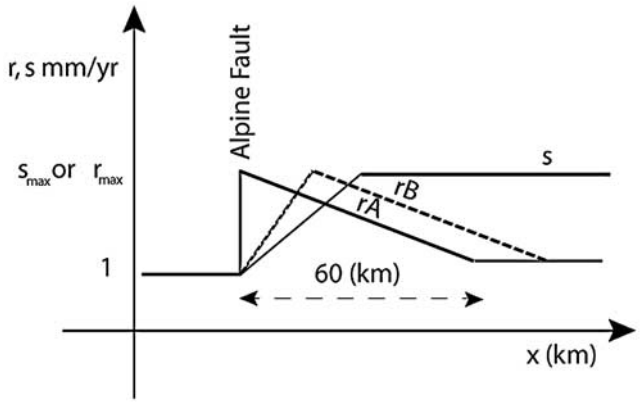

Figure 1. Tectonic models adopted here. Here r is the vertical rock uplift velocity function; s is the horizontal advection velocity function; rA depicts the case where the maximum rock uplift is near the fault; and rB is where the maximum rock uplift is away from the fault.

of the thin plate and is taken equal to 30 km for the Southern Alps of New Zealand, following *Stern* [1995]. The load $q(x,y)$ is given by

$$q(x,y) = zg\rho_c + hg\rho - wg\rho_m \tag{16}$$

where ρ, ρ_c and ρ_m are respectively the density of the ice, the crust and the mantle, z is the height of the landscape (bedrock), and h is the ice thickness. For computational efficiency, we assume that the elastic thickness and properties are uniform in space and time, in which case equation (14) can be solved by a very efficient spectral method [*Nunn and Aires*, 1988].

[19] Note that equation (14) is based on the assumption that the mantle underlying the elastic plate is inviscid. This is a valid assumption when treating problems on geological timescales, i.e., over millions of years. However, in the situation considered here, where removal of surface material, and thus loading-unloading, takes place at a much faster pace, i.e., over tens of thousands of years, this assumption is not strictly valid. To treat this problem as is done in studies of postglacial isostatic rebound [e.g., *Johnston*, 1993] by including the effects arising from the viscous flow in the asthenospheric mantle would be impractical here as it would unreasonably increase the computational cost of the isostatic calculations. In interpreting the results presented here, one must therefore keep this limitation of the model in mind.

2.4.2. Tectonic Rock Uplift and Horizontal Advection

[20] In order to determine the impact of the tectonic rock uplift and horizontal advection, a tectonic component is added to the model. The approach adopted here is kept very simple. We first impose a vertical velocity field to the surface to simulate tectonic rock uplift. Two alternative tectonic models will be tested here (see Figure 1 and the discussion in the section devoted to the Southern Alps of New Zealand). In the first one, we assume that the vertical rock uplift is maximum in the vicinity of the major thrust of the collision, known as the Alpine Fault. For the second end-member model, we assume that the tectonic rock uplift is maximum in the central part of the mountain belt.

[21] We also allow for the surface to be advected by tectonic horizontal transport, but we assume that the vertical rock uplift and horizontal transport are independent of each other. They are clearly linked by the geometry of the underlying Alpine Fault and its continuation at great depth, but this geometry is relatively poorly constrained. Furthermore, the deformation of a crustal block moving along a curved or segmented thrust or normal fault is not known either, as demonstrated by the wide range of kinematic models used to represent it [e.g., *Dulla*, 1991; *Verral*, 1981; *White et al.*, 1986; *Williams and Vann*, 1987; *Braun et al.*, 1994]. The horizontal advection is thus imposed by a simple function (see Figure 1) and treated by first advecting the grid on which the topography is calculated and then interpolating it back onto an undeformed grid used in the finite difference scheme. This has the disadvantage of including some numerical diffusion. However, in cases where diffusion (representing hillslope processes) is an active land-forming mechanism, the numerical diffusion becomes negligible and this artifact therefore does not substantially affect the numerical experiment.

2.5. Modeling Approach

[22] The shallow ice approximation (SIA) has the advantage of considerably reducing the complexity of the equations of the model. It therefore permits fast and efficient computation of the ice thickness. Although it has been applied to tectonically growing orogens [*Tomkin and Braun*, 2002], it limits the applicability of the model to regions with small vertical gradients, which is certainly not the case in mountainous areas, unless a coarse grid is used (>1–3 km). One way to circumvent this limitation is to solve the full three-dimensional equation for the ice flow [e.g., *Pattyn 2003*]. This is, however, not computationally viable at the scale of a mountain range and can only be used to model the evolution of small glaciers. Another approach is to solve equation (4) on a low-resolution grid, which respects the SIA, and then interpolate the results onto a high-resolution grid to estimate the erosion rates. This method is justified since the erosion law is proportional to the sliding velocity (equation (9)), the sliding velocity is proportional to the slope of the ice surface (i.e., $z+h$) and the ice surface is smooth (as it is the solution of a diffusion-type equation) and, consequently, not affected strongly by an interpolation. This is the method we adopt here as shown in Figure 2. We start with a high-resolution digital elevation model (resolution of ~250 m) to define the initial topography ($z_{highres}$). We then extract a low-resolution grid of resolution ~ 2000 m, (z_{lowres}), on which we apply a Gaussian smoothing operator to avoid large vertical gradients. In this way, the topography used to calculate the ice thickness respects the SIA. The ice thickness and velocities are computed on this coarse grid until a steady state with the climate is reached. We then use a linear interpolation to define the ice thickness on the high-resolution grid ($(h+z)_{high\ res}$ and $u_{s,highres}$), noting that where $z_{highres}$ is greater than $(h+z)_{highres}$ the sliding velocity is set to nil. Finally, the erosion due to glacial, hillslope and river processes is computed on and applied to $z_{highres}$. The process is then repeated for each time interval of 200 years. This approach has several advantages. It provides us with a better tool to establish ice extent reconstruction. It also permits us to assess with greater detail which parts of the

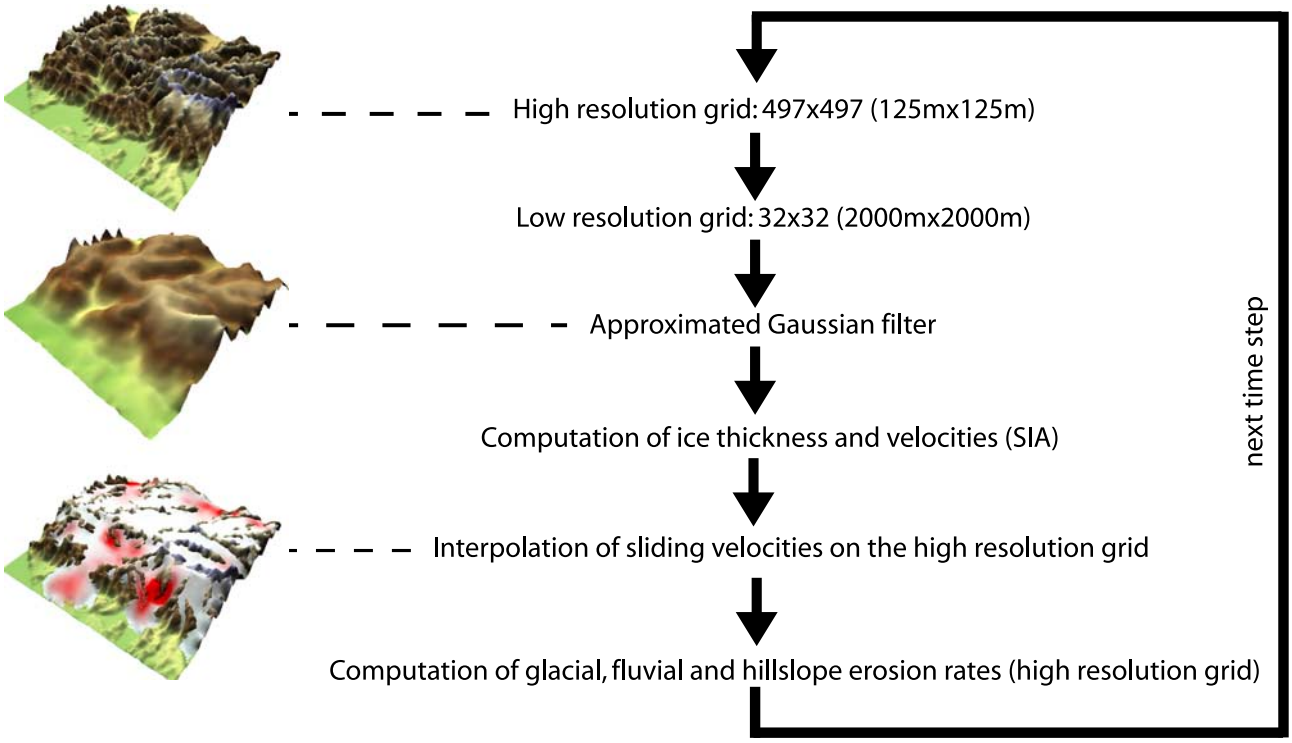

Figure 2. Modeling approach (see text for details).

landscape have been affected by fluvial or glacial erosion. Finally, we can now compute erosion in regions where slopes and relief are substantial.

[23] We also decided to apply the model on an existing digital elevation model (DEM). The choice of using an existing DEM is mainly three folds. First, by using the digital topography we can compare, to a first-order, ice volume/geometry to mapped past glacial extents. This is actually the only way we can calibrate the model at the timescale of interest. Second, we can estimate spatial patterns of erosion and, in turn, produce erosion maps that can be confronted to field observations. Finally, in contrast to statistical analysis of DEMs [e.g., *Brocklehurst and Whipple*, 2002], we can directly test the different physical assumptions of the model to extract first-order characteristics of a glaciated landscape. Note that by using the DEM as initial conditions, we do not intend to find the conditions that led to the present-day topography but rather try to assess the current state of the topography and its evolution in the future.

2.6. Model Limitations

[24] Although our parameterization of glacial erosion is based on well-founded physical mechanisms and lead, as shown below, to the simulation of the large-scale features of the evolution of a fluvioglacial system, several improvements could be made to the model that would render its predictions more directly comparable to natural, glaciated landforms. For example, the assumption that the temperature within the ice is at steady state is too simplistic. Transport of glacial debris and sedimentation should be included. More importantly, periglacial processes should be treated accurately, as they are currently ignored and incorporated in a very ad hoc manner within the diffusion term of equation (13). These must be important, particularly to maintain peaks at reasonable altitudes. Landslides are not explicitly computed. Subglacial hydrology is not addressed. Finally, phase changes between water, snow and ice are not explicitly modeled. The implications of some of these limitations will be discussed in the light of the modeling results.

3. Southern Alps of New Zealand

[25] We wish to apply the model to a geological situation. The Southern Alps of New Zealand is a perfect example of an orogen that has been affected by both fluvial and glacial erosion. In this section, we start by outlining our current knowledge of the past ice extent and the climate history of the Southern Alps. We then briefly outline the tectonic setting and the regional geomorphology of the Southern Alps. In the following section we will apply the model to this mountain range.

3.1. Last Glacial Maximum and Past Climate in the Southern alps

[26] In the Southern Alps of New Zealand, the glacial history and climate evolution during the Quaternary have been established mainly from mapping of the extent of the ice at the Last Glacial Maximum (LGM) [e.g., *Suggate*, 1990; *Suggate and Almond*, 2005] and analysis of marine sediments [e.g., *Nelson et al.*, 1993]. These observations suggest that the Pliocene glaciations have been initiated about 2.5 ± 0.1 Ma. Nine glaciations have been documented in the South Island in the past 0.7 Ma, with four of them during the last 0.35 Ma [*Suggate*, 1990; *Nelson et al.*, 1993; *Suggate and Almond*, 2005].

[27] Owing to the apparently high sensitivity to climate changes of the glaciers in New Zealand, coupled with high rock uplift and exhumation rates, it is difficult to establish a complete glacial history reconstruction. Consequently, only the last glaciation can be studied with some confidence. *Suggate and Almond* [2005] reported three major advances during this period (at 28, 21.5 and 19 ka), each of them being regarded as representative of the LGM. These glacial advances were followed by a massive and rapid retreat of glaciers beginning ~14 ka. This retreat rapidly led to ice volumes comparable to those observed today. This retreat is thought to be associated with a regional increase in world sea level temperature varying between 4 and 8°C [*Porter*, 1975; *Soons*, 1979; *Barrows et al.*, 2000]. These observations can also be correlated with changes in global sea level [*Lambeck et al.*, 2002] and inferences on the world ocean mean temperature from the Vostok ice core in Antartica [*Petit et al.*, 1999; *EPICA community members*, 2004].

[28] Not many studies have documented the variations of the equilibrium line altitude (ELA) in New Zealand in response to climate change during the Pleistocene. *Porter* [1975] reported the present and past position of the ELA for a few glaciers of the eastern part of the orogen and in the Ben Ohau range (~50 km southeast from Mount Cook). He showed that large changes in the ELA position have taken place between the LGM and today (up to 900 ± 50 m). *Chinn* [1995] focused on contemporary glaciers and reported glacier volume fluctuations from snow line elevations. This study clearly documented a large variation of the ELA across the mountain belt, varying from 1600m on the western side to 2300 m for the easternmost glaciers. This work was complemented by that of *Fitzharris et al.* [1997] who showed that atmospheric circulation exerts a strong control on glacier mass balance and, in turn, on the position of the ELA. Although current precipitation patterns do not always reflect past climate, it is thought that the asymmetric pattern observed in the Southern Alps today existed during Pliocene and Pleistocene glaciations [e.g., *Soons*, 1979; *Chamberlain et al.*, 1999] and was therefore responsible for the asymmetry in ELA variations. Finally, it is also accepted that there is a close correlation between the glacial sequences on either sides of the orogen [*Gage and Suggate*, 1958] implying that the orographic effect is not sufficient to prevent major ice advances/retreats on either side of the orogen.

3.2. Tectonic Model of the Southern alps

[29] The Southern Alps of New Zealand are the result of ongoing oblique convergent motion between the Pacific and Australian plates along a major structure known as the Alpine Fault [e.g., *Walcott*, 1998]. This tectonically active mountain range is often cited as the classical example of a two sided orogen [*Koons*, 1990] where material is accreted on the pro side and rapidly exhumed on the retroside (adopting the definitions introduced by *Willett et al.* [1993]). The simplicity of the collision and the rapidity with which convergence and exhumation are occurring make it an ideal natural laboratory to explore the effects of climate oscillations on the spatial patterns of erosion.

[30] Early studies to constrain the patterns of rock uplift and exhumation suggested that the velocity of the convergence motion between the two plates increases in the vicinity of the Alpine Fault [*Kamp and Tippett*, 1993; *Tippett and Kamp*, 1993; *Norris and Cooper*, 2000]. These results have been questioned [*Walcott*, 1998; *Batt and Braun*, 1999; *Little and Holcombe*, 2002; *Little et al.*, 2005; J. Braun et al., Strain localization in a linear Newtonian fluid and the formation of narrow plate boundaries, submitted to *Earth Planetary Science Letters*, 2007]. For instance, *Little and Holcombe* [2002] reported that the sense of shear observed in the ductile fabric is unequivocal and implies a relative motion (thrusting) that requires a decrease in the relative velocity toward the Australian plate. Recently, Braun et al. (submitted manuscript, 2007) also argue that the convergence motion must decrease toward the Alpine Fault. To help illuminate this debate, we shall test these two competing models in this study.

3.3. Regional Geomorphology of the Southern alps

[31] *Adams* [1980] was first to point out that the main features of the landform in the Southern Alps result from the combined alternating action of fluvial and glacial erosion. *Whitehouse* [1987] divided the landscape of the Southern Alps into three different regions: (1) an ''old glacial landscape'' on the southeastern side of the mountain range, (2) a recently glaciated landscape in the central part (characterized by the presence of steep backwalled cirques) and (3) a fluvial-dominated landscape on the western side of the main divide (where V-shaped valleys have formed in response to intense fluvial dissection, landsliding, and rockfall-snow avalanching). *Hovius et al.* [1997] described the western side of the mountain belt as characterized by ''dissected, rectilinear slopes, frequently steeper than 45 and with thin (<1 m) regolith cover'' where the dominant mass transport mechanism is landsliding triggered by bedrock channel incision. Recently, Herman and Braun [2006b] further described the complexity of the landscape. In their study, they presented a detailed qualitative description, based on DEM and satellite image analyses, of the different processes acting on the west coast of the Southern Alps, where precipitation and exhumation are maximized. They illustrated that today's landscape on the west coast is clearly in a transitional stage between glacial forms and nonglacial forms as illustrated in Figure 3. The erosional processes vary from fluvial transport on gravel beds in the lower parts of the western slopes to fluvial incision and glacial erosion in the upstream regions. This description is in fact very similar to the one described by *Whitehouse* [1987]. Using a numerical model of a fluvial landscape evolution (Cascade [*Braun and Sambridge*, 1997]) combined with an appropriate inversion technique (the Neighborhood Algorithm [*Sambridge*, 1999]), *Herman and Braun* [2006b] also showed how the landscape is currently responding to cyclic glaciations and rapid tectonic rock uplift. Their numerical analysis highlights the role of hillslope diffusion and places emphasis on the significance of river tributaries during the glacial retreat. They concluded that the transition from glacial to interglacial states leads to a rapid reshaping of the landscape and to a reduction of the ridge to bottom relief. Consequently, most parts of the landscape on the west coast will never reach a steady state during an interglacial period since a colder glacial period will return. Similarly, recent field observations [*Herman and Braun*, 2006b] also suggest that two regions of the west coast have not

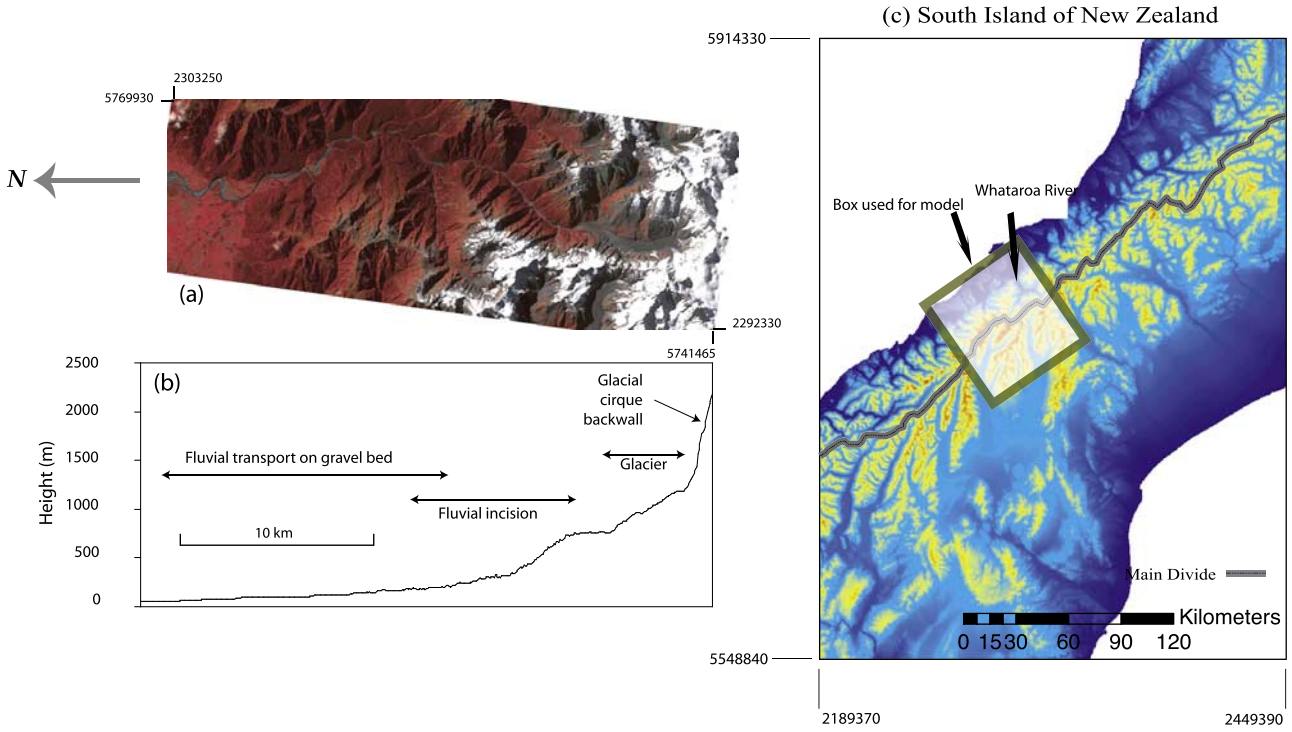

Figure 3. (a) Advanced Spaceborne Thermal Emission and Reflection Radiometer (ASTER) (1B) image of the Whataroa River. (b) River profile of the Whataroa River and description of the key mechanisms at play (modified from *Herman and Braun* [2006b]): fluvial transport in the downstream part, fluvial incision in the central part, and glacial erosion in the most upstream part. (c) Digital elevation model of the South Island of New Zealand (50 m resolution, data from Terralink International Limited). New Zealand map grid system is used for the coordinates.

recovered from the last glaciation: the upper part of the western face that is still covered by ice and the lowest section of the valley that is still filled with several hundreds of meters of sediments (T. Stern personal communication, 2005). Here we continue this analysis of landform evolution in a rapidly evolving climatic and tectonic environment by considering the effects of glacial erosion.

4. Modeling Results

[32] The modeling results are presented in Figures 4 to 11. In the first part of this section, we demonstrate how the computed ice thickness evolves in space and time across the mountain range in response to climate changes (experiment 1). In the second part, we present solutions in which erosion, tectonic rock uplift and horizontal advection have been included (experiments 2 to 7). The common set of parameters used in all simulations is presented in Tables 1 and 2.

4.1. Evolution of the Ice Cap on a Steady Topography (Experiment 1)

[33] The aim of this first simulation is to assess the ability of the model to represent the glacial history of the Southern Alps before attempting to estimate the resulting glacial erosion patterns. We present the results of these simulations in Figures 4 and 5. At each time step of the experiment, the climate (through the assumed atmospheric temperature) is set to vary between its coldest stage (corresponding to the LGM) and its present-day value, and the model is run until a near steady state is achieved for the given climatic conditions. In this first experiment, we consider a uniform snowfall pattern across the mountain range (no orographic effect is considered). There is no erosion, tectonic rock uplift or horizontal advection at this stage. The high-resolution grid has a uniform spacing of 125 × 125 m and the low-resolution one of 2000 × 2000 m. The ice and climate parameters are selected to simulate an ice extent comparable to the mapped LGM extent of terminal and lateral moraines (Table 1). The sliding and deformation velocity constants are chosen to produce realistic velocities (i.e., within an order of magnitude of estimates of ice velocities in modern glaciers, $\sim$0–200 m a^{-1} [e.g., *Kaab*, 2002]).

[34] Parameter values can be adjusted to obtain results that compare relatively well with field observations of the mapped LGM ice extent (Figure 4). For example, a large piedmont-type glacier emerges from the Whataroa-Perth catchment. However, the volume of the ice flowing along the Franz Josef valley is slightly smaller than deduced from field observations.

[35] In Figure 5, we display the results of the computation by plotting the high-resolution topography on which we superimpose the calculated ice thickness. The ice shaded by the magnitude of the computed sliding velocity at the ice-bedrock interface, with red areas corresponding to regions of fastest ice movement. Mean sea level temperature is assumed to vary by 5°C between modern sea temperature in January of $\sim$17°C [*Levitius and Boyer*, 1994] and LGM conditions. Climate variation between each experiment in Figure 5 therefore corresponds to a change in mean sea level temperature of 1°C. We also estimated the ELA for each

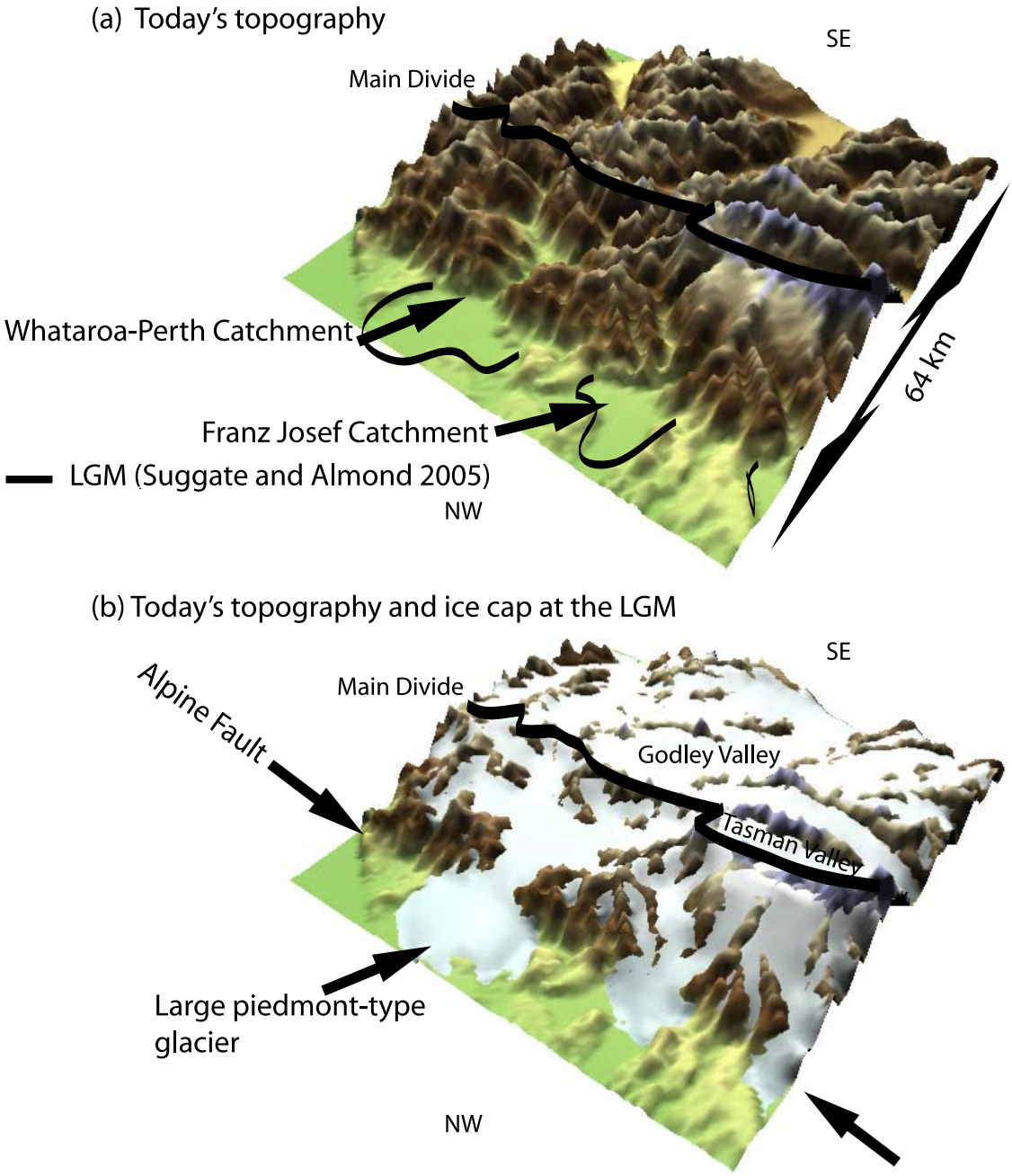

Figure 4. (a) Current topography and position of the LGM moraines from *Suggate and Almond* [2005]. (b) Simulated LGM ice cap on the topography (see text for explanation). Note that the vertical scale was exaggerated for the clarity of Figure 4 and Figures 5–12.

step by computing the mass balance as a function of altitude as shown in Figure 5g.

[36] For the warmest climate (i.e., close to present day), or the smallest ice cap (Figure 5a), the ice cover is limited to the highest regions as expected. The model cannot reproduce the details of the existing glaciers but, nevertheless, the general pattern of ice cover is comparable to the present day. A reduction of the mean sea level temperature (Figures 5b to 5f), corresponding to a decrease of the ELA, logically induces an extension of the ice cap. Interestingly, the ice appears to extend first on the southeastern side of the divide. This is simply because that is where the mean altitude is highest. On the northwestern slopes, the portion of the landscape covered by ice for each time step (and consequently each ELA value) exhibits a more complicated pattern. In Figure 5c, the ice is flowing down to low altitudes near the Franz Josef area. It also covers a large part of the Whataroa River, but most of the Perth River is still ice free. This is just a consequence of the geometry of the range. Indeed, the upper parts of the Whataroa River and Franz Josef areas correspond to a region where the drainage divide is highest and closest to the Alpine Fault. Consequently, large amounts of ice accumulate above the ELA and, in turn, flow downward. As the ELA decreases, the

Table 1. Parameter Values Used to Compute Ice Thickness

Parameter	Value	Definition
B	1×10^{-16} Pa^{-3} a^{-1}	flow law parameter
B_s	5×10^{-9} Pa^{-3} a^{-1} m^{-2}	sliding law parameter
p	3	Glen's flow parameter
ρ	910 kg m^{-3}	density of ice
g	9.81 m s^{-2}	gravitational acceleration
G	110 mW m^{-2}	geothermal gradient
K	9.828 W m^{-1} K^{-1}	thermal conductivity
κ	$\frac{G}{\rho 2115}$	thermal diffusivity
λ	43.5	latitude
k_c	100 km	constriction constant
α	0.01 C cm^{-1}	lapse rate
γ_1	1.0	arbitrary constant
γ_2	0.2	arbitrary constant

Perth River also becomes covered by ice and, ultimately, both the Perth and Whataroa ice streams join to form a large piedmont-type glacier, as shown in Figures 5f and 4b.

[37] A close examination of the sliding velocity already provides information on where the model predicts glacial erosion, remembering that the ice is only sliding and thus eroding where the melting point has been reached at the ice-bedrock interface. Figures 5a to 5c show that for a small ice cap the ice is mostly sliding where the greatest slopes are found. On the southeastern side, as the ice cap grows, the regions where melting and thus erosion takes place evolve progressively from the upper reaches of the large valleys to their lowermost parts. This has important consequences for estimating erosion patterns in response to climate changes. It suggests that the ice focuses erosion in different regions of a mountain belt as the ice cap evolves. On the northwestern side, where the slopes are the greatest, the erosion pattern also evolves from the summit to the valley bottoms but the model also predicts that, at the glacial maximum, very high ice sliding velocities are found on the sides of interfluves or valley walls (Figure 5f). This would result in the formation of aretes and U-shaped valleys typical of glaciated landscapes.

[38] This simple experiment also shows that most of the areas of high sliding velocity are found on the northwestern side of the range. This would therefore imply that focused erosion on the western slopes may simply result from the asymmetrical geometry of the mountain belt and does not require an orographically controlled precipitation pattern of snow, as previously suggested by *Tomkin* [2000]. It is also worth noting that the predicted patterns of basal ice melting/sliding display a definite clustering which evolves through time and is thus different for each stage in the climate evolution. This would therefore imply that (1) erosion by glaciers is not as uniform as by rivers and (2) local overdeepening is common. This is a very important result because it suggests that climatic oscillations will control and rapidly modify erosion patterns and are thus likely to prevent the topography from ever reaching an equilibrium. Finally, it is important to realize that the location of where the ice starts sliding or where the sliding velocity is greatest, and consequently where the erosion is maximized, does not necessarily correspond to the location of the ELA as suggested by, e.g., *Anderson et al.* [2006].

[39] Although the model (and more specifically the SIA) dictates that the velocity of the ice is in the direction of maximum slope of the ice surface, it appears that the computed velocities are also aligned with the direction of maximum slope of the bedrock topography. This is simply because the predicted ice divide matches with the topographic divide everywhere. This implies that the ice will flow away from the main topographic divide and glacial erosion cannot be called upon as an efficient mechanism for topographic divide erosion and/or migration. This prediction must, however, be treated with caution because the ice cap is computed on a coarse grid. Local mismatches between topographic and ice divides should therefore not be excluded at a length scale smaller than 2 km. The calculations also suggest that the ice cap is not large enough to completely cover the highest peaks of the mountain range. This observation could be tested with quantitative techniques, for example using OSL or cosmogenic dating or field mapping of trimlines.

4.2. Glacial Erosion Patterns in Response to Tectonic Forcing

[40] The purpose of this second series of model experiments is to assess the influence of specific assumptions concerning the erosion laws that are applied. The questions we wish address here are: where is the erosion spatially focused in response to tectonic forcing? and what are the main erosive mechanisms predicted by the model in the different parts of the landscape and at different time during a glacial cycle? In the following simulations we thus include the feedbacks from erosion and tectonic rock uplift and advection. We start from the present-day, "real" topography, using a high-resolution grid of 250 $\times$ 250 m and try to estimate the landscape's response to varying assumptions on the erosional parameters. Each simulation lasts for 360 ka. For consistency and ease of comparison, we use similar parameters to describe the peak conditions (minimum and maximum glacial extents) as those of experiment 1 (see Table 1) and assume cyclic climatic variations with a period of 120 ka (to roughly approximate glacial cycles [*EPICA community members*, 2004]). thus each cycle corresponds to an increase in mean sea level temperature of $\sim$ 5°C for

Table 2. Erosion Parameters Used for Each Experiment[a]

Experiment	Tectonic Model	K_g, a^{-1}	K_f, a^{-1}	D, m^2 a^{-1}	C_1, m^2	C_0, a^{-1}	r_{max}, mm a^{-1}	s_{max}, mm a^{-1}	Cycle
Experiment 2	A	10e-3	5.0e-6	1.0	3.5e5	1.0e7	8.0	8.0	yes
Experiment 3	A	10e-3	7.5e-6	1.0	3.5e5	1.0e7	8.0	8.0	yes
Experiment 4	A	7.5e-3	5.0e-6	1.0	3.5e5	1.0e7	8.0	8.0	yes
Experiment 5	A	20e-3	7.5e-6	1.0	3.5e5	1.0e7	8.0	8.0	yes
Experiment 6	B	10e-3	7.5e-6	1.0	3.5e5	1.0e7	8.0	8.0	yes
Experiment 7	B	10e-3	5.0e-6	1.0	3.5e5	1.0e7	8.0	8.0	no

[a]Read, for example, 10e^{-3} as 10×10^{-3}.

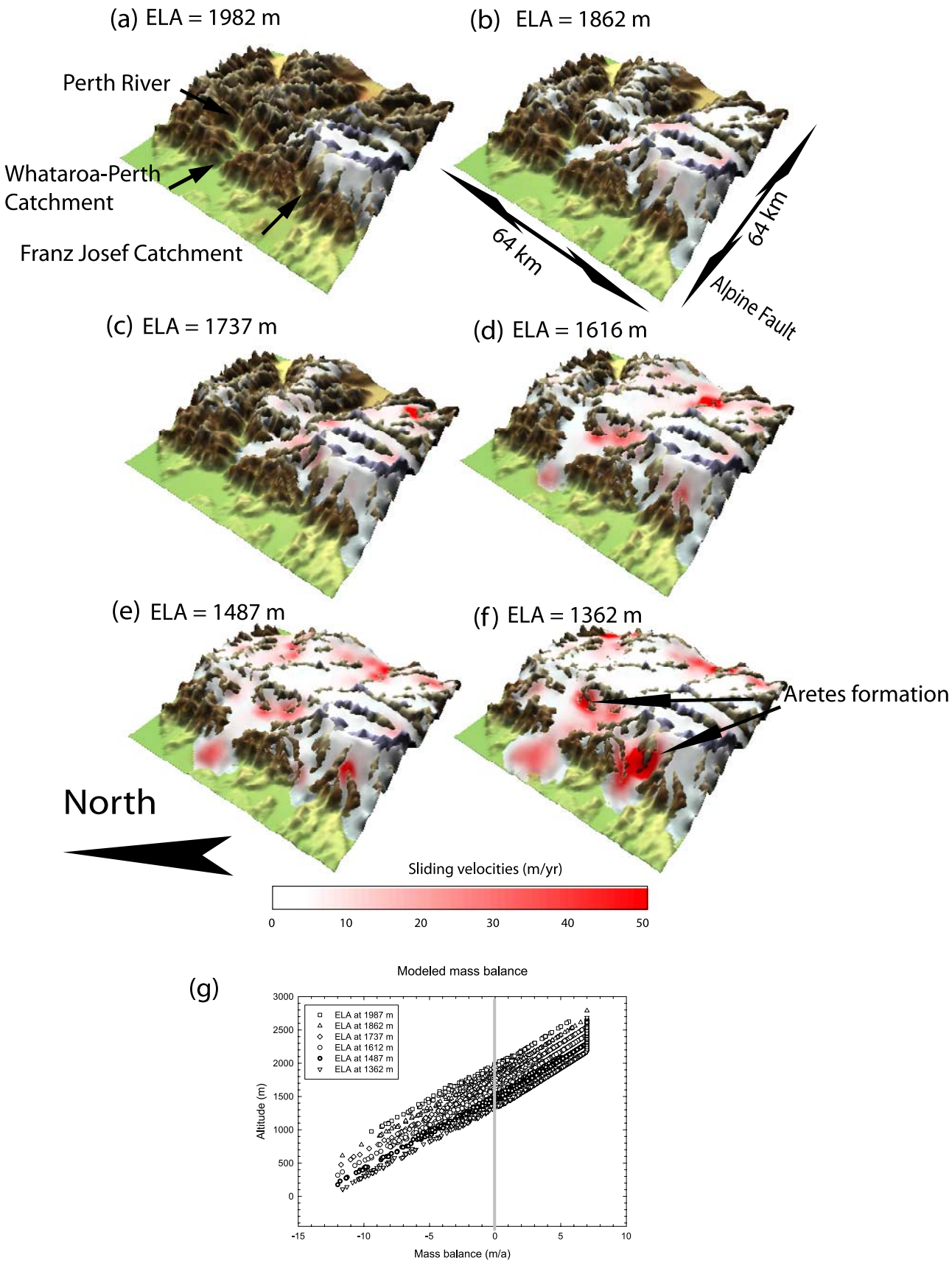

Figure 5. Experiment 1 showing ice caps and calculated sliding velocities for different ELA. (a)–(f) Simulated ice caps with fixed climates. (g) Computed mass balance curves.

20 ka, followed by a decrease of ~5°C during the following 100 ka.

[41] The set of parameters used for each model simulation/experiment is summarized in Table 2. We also test two different tectonic models as described above: tectonic model A, in which the rock uplift rate increases from southeast to northwest and is maximum near the Alpine Fault (experiments 2 to 5) and tectonic model B, where the rock uplift rate increases from southeast to northwest, is maximum 15 km away from the Alpine Fault and then decreases toward the fault (experiments 6 and 7). Experiment 2 examines the landform response for a first set of parameters which is chosen as the reference experiment for the discussion; experiment 3 corresponds to an increase of the fluvial erosion constant, K_f; experiment 4 explores the behavior of the model when the ice erosion constant, K_g, is decreased with respect to the reference experiment; experiment 5 addresses the case of an increase of glacial erosion efficiency through K_g; experiment 6 has the same erosion parameters than experiment 2 but investigates the effect of the tectonic experiment B; and experiment 7 is the same as experiment 6 except that the climate is assumed to be constant at its coldest stage. All these experiments include the effects of orographically controlled precipitation, supposing westerly winds. As already shown by *Koons* [1990], we cannot find an adequate fluvial erosion constant that would allow the model to evolve toward an acceptable topography (i.e., where the topography is lowest near the Alpine Fault) if the orographic effect is not included in the model.

4.2.1. Experiment 2

[42] The experiment starts with present-day topography as shown in Figure 6a. Figures 6b to 6d show the evolution of the topography with time. After the first cycle (i.e., 120 ka, Figure 6b), the large valleys on the southeastern side of the divide are deeply incised by glaciers. Some ridges are also locally eroded, as a consequence of flow of ice over local saddles. The drainage network on this side of the divide can therefore be characterized as not stable during the early stages of the experiment. This is, in part, because the rock uplift rate on the southeastern side of the divide is relatively small. We propose that this could explain why the geometry of valleys on this side of the divide is easily controlled by faults [*Herman and Braun*, 2006b]. On the northwestern side of the divide, large glaciers can flow and incise along the valley floors of the Whataroa and Perth Rivers. This, in turn, produces valleys characterized by relatively flat longitudinal profiles. In their downstream sections, the glaciers can erode very efficiently, even beyond the Alpine Fault. In their upper parts, they create glacial backwalls. Erosion of the interfluves seems to be dominated by river incision and hillslope processes (diffusion) near the Alpine Fault and to oscillate between glacial and fluvial erosion within the higher parts of the landscape. A closer look at the ice extent presented in Figure 5 actually shows that the interfluve slopes at the mouth of the Whataroa-Perth catchment are ice free and thus, for most of their evolution, exposed to fluvial and hillslope erosion; on the contrary, wet-based glaciers flow along the main valley trunks. Alternatively, near the Franz Josef and Fox Glacier areas (on the same side of the divide), the ice cover is generally more complete and glacial processes appear to be the dominant erosion mechanisms everywhere. The ice cover is more extensive in this area because of the higher mean elevation, which results in larger accumulation areas and the formation of ampler glaciers that can flow down to low elevations.

[43] After the second cycle (i.e., 240 ka, Figure 6c), the large valleys on the southeastern side are maintained. There the glaciers and, more precisely, their longitudinal profiles are now close to their steady state forms. On the northwestern side of the range, the drainage network is kept very similar to the initial network. There is still substantial glacial erosion in both Whataroa-Perth and Franz Josef–Fox areas along the main trunks. Fluvial and hillslope erosion remain the main erosion mechanisms at the mouth of the Whataroa-Perth catchment.

[44] After the third cycle (i.e., 360 ka, Figure 6d), the erosion patterns are very similar to those of the previous cycles. A slight migration of the drainage divide toward the Alpine Fault is observed in the Whataroa-Perth catchment, but the drainage network is not modified as the experiment progresses. However, there is not enough erosion in the direct vicinity of the Alpine Fault leading to the formation of an internal drainage basin which prevents the model from running for an additional cycle. At the end of the experiment, the landscape is less realistic. The drainage density is too low, the landscape is not sufficiently incised. Note also that erosion along some valleys near the edge of the mesh is influenced by the choice of the boundary conditions.

4.2.2. Experiment 3

[45] In this experiment, we investigate the effect of increasing the fluvial erosion constant, K_f. The results are summarized in Figures 7a–7d. After 120 ka of evolution (Figure 7b), the erosion patterns on the southeastern side of the range are very similar to those produced in experiment 2. This is because the role of fluvial incision in this part of the range is minimal. On the northwestern slopes, discrepancies with the reference experiment rapidly develop. The incision of the main river tributaries is considerable in the parts of the landscape that are exposed to fluvial erosion which results in a lowering of the interfluve ridges and, in turn, a reduction of the part of the landscape where ice accumulates (i.e., the number of integration points higher than the ELA declines). This leads to a reduction of the ice flow along the main trunks and, consequently, less material is eroded by glaciers. This situation is most marked in the Whataroa and Perth river area; in the Franz Josef–Fox area where fluvial erosion is less extensive, the mean elevation remains high enough to preserve most of the ice volume and consequently, the glacial erosion rates remain comparable to the reference experiment.

[46] After 240 and 360 ka (Figures 7c and 7d), the model predictions on the southeastern side remain similar to those of experiment 2, whereas the topography keeps evolving differently on the northwestern side. In the Whataroa-Perth catchment, the mean elevation in the upstream parts of the catchment progressively increases. This induces a widening of the ice accumulation area which triggers an enhanced flow of ice that is now sufficiently large to erode material at lower elevations. This, in turn, leads to the formation of an overdeepening and a water sill. When the ice retreats at the end of a glaciation, this overdeepening should fill up with glacial debris. However, the model is limited by the fact that it does not include glacial transport or sedimentation, and,

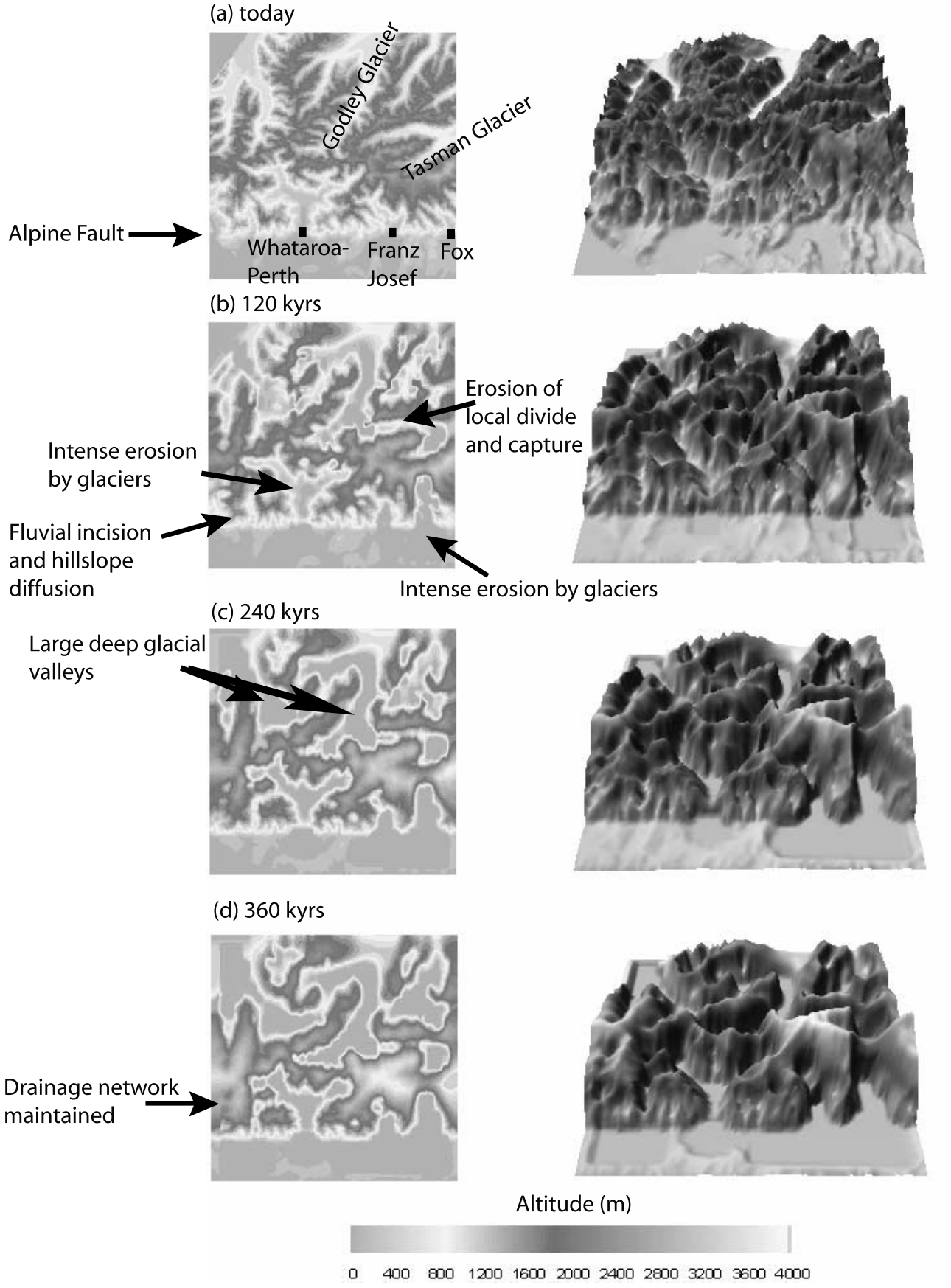

Figure 6. Experiment 2 showing (left) plan views and (right) perspective views of the topography. (a) Present-day topography. Evolution of the topography after (b) 120, (c) 240, and (d) 360 ka.

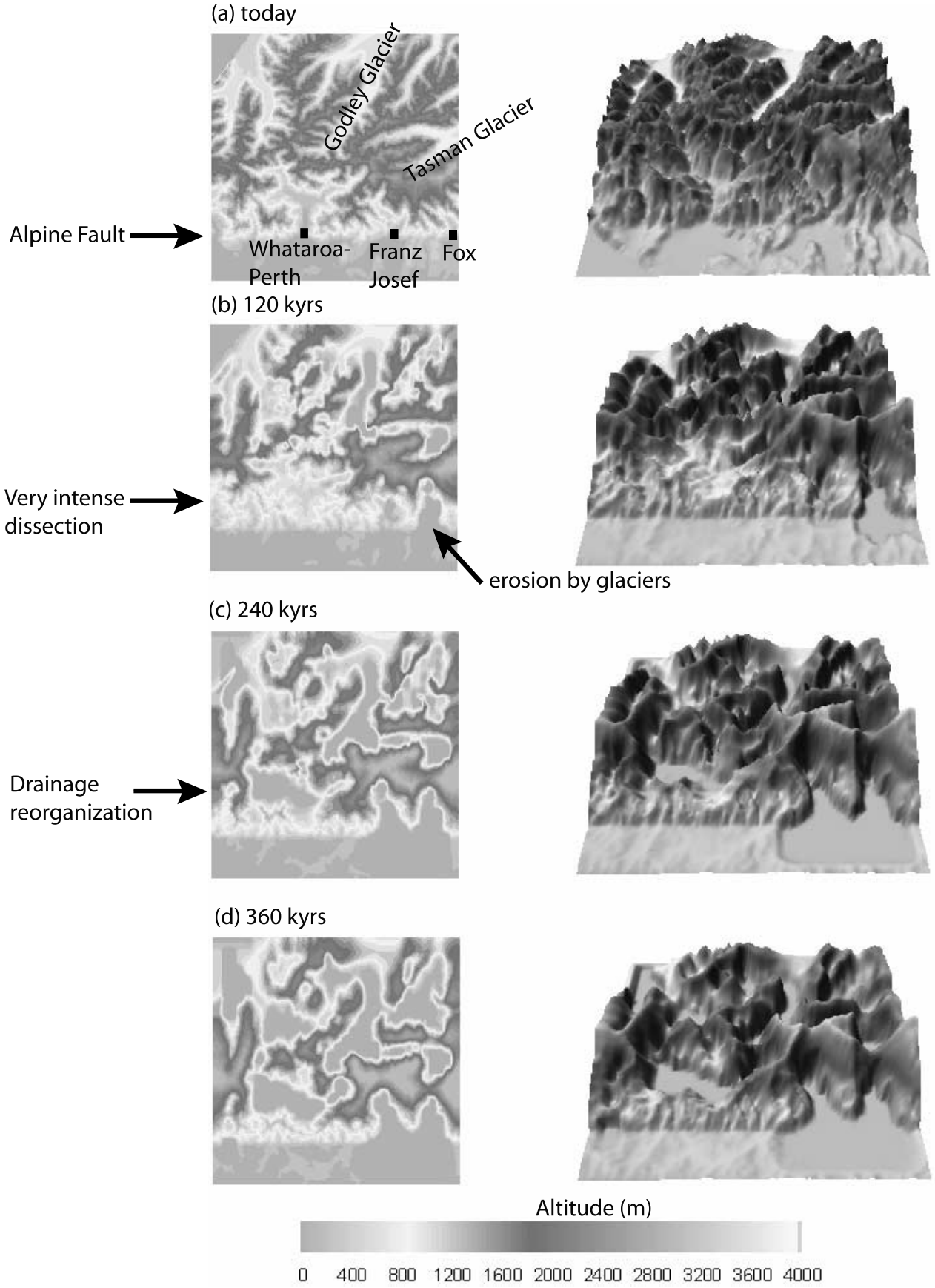

Figure 7. Experiment 3 similar to Figure 6. The value of the fluvial erosion constant, K_f, has been increased with respect to experiment 2.

consequently, cannot predict the formation of deep postglacial sedimentary troughs in these overdeepened regions.

[47] Another important difference between this experiment and the reference experiment is the onset of drainage network reorganization during the third simulated glaciation, especially in the lower parts of the Whataroa catchment (Figure 7c). This is a direct consequence of the imposed increase in the fluvial erosion constant. Finally, in the Franz Josef–Fox area, the model predictions are similar to the reference experiment, because glacial processes continue to dominate throughout the experiment in this part of the landscape.

4.2.3. Experiment 4

[48] In this experiment, we explore the impact of decreasing the efficiency of glacial erosion, K_g, on the evolution of the topography. The results are presented in Figure 8. We again compare these results to those of experiment 2.

[49] After the first cycle (Figure 8b), the geomorphology predicted by the model on the southeastern side is equivalent to experiment 2. This suggests that, on this side of the divide, the evolution of the topography is not very sensitive to a change of the erosional efficiency of the glaciers. On the northwestern side of the divide, the erosion by glaciers in the Whataroa-Perth and Franz Josef–Fox areas is also analogous to the reference experiment.

[50] After the second and third cycles (Figures 8c and 8d), the erosion patterns are still similar to experiment 2 on the southeastern side. This confirms that on this side of the divide, the evolution of the landscape is less sensitive to a change of erosion efficiency. In contrast, some differences emerge on the northwestern side. Some ridges that were progressively eroded away by the ice in experiment 2 are now preserved while others have disappeared. The most noticeable difference comes from the northwestern side of the orogen: the erosion rate is not sufficiently high at the mouth of the Whataroa-Perth catchment to counteract the rapid rock uplift rate just southeast of the Alpine fault. This is because the period over which the glacier flows across the Alpine Fault is not sufficiently long to lead to a mean erosion rate that exceeds the rock uplift rate, whereas higher up within the catchment, the glaciated period is long enough for mean glacial incision rates to be comparable to the rock uplift rates.

4.2.4. Experiment 5

[51] We now look at the effects of increasing the glacial erosion efficiency by doubling K_g with respect to the reference experiment. The results of this numerical experiment are shown in Figure 9.

[52] After the first cycle (Figure 9b), much larger amounts of material are eroded on both sides of the divide in comparison to the reference experiment. Most of the valleys are widened and overdeepened. On the southeastern side of the divide, differences from the reference experiment are clearly noticeable: there is much more erosion occurring. The width and height of glacial valleys are sensitive to this increase in K_g. This is because glacial erosion rates are higher, and the subsequent landform that is formed cannot be renewed on the timescale of a glacial cycle. The drainage network is also more stable on that side of the divide than it is in the reference experiment, since no valley capture is observed. On the northwestern side of the range, erosion rates are much higher in both the Whataroa-Perth and Franz Josef–Fox areas. The valleys are substantially widened and large parts of the landscape are brought down to low elevation.

[53] After 240 ka (Figure 9c), the erosion patterns are very similar to those of the first cycle. The wide valleys that were formed on both sides of the divide are preserved. The large regions that were eroded down to low altitude remain low. After 360 ka (Figure 9d), the lowering of the mean altitude (in comparison to the reference experiment) results in a reduction of the size of the accumulation area in the upper parts of the Whataroa-Perth catchment, which, in turn, reduces the flow of ice downstream. Consequently, there is not enough erosion at the mouth of the catchment to compete with the high rock uplift rate, which induces the formation of a ridge on the up-throw side of the Alpine Fault and stops the flow of ice.

[54] This results demonstrates that the value of the ice erosion parameter, K_g, is relatively well constrained by the direct consequences of either lowering (experiment 4) or increasing it (experiment 5); decreasing its value leads to insufficiently low erosion rates near the Alpine fault; increasing it leads to lowering of the accumulation areas, reduction in ice flow and a similar result: an unacceptable decrease in erosion rate near the Alpine Fault. Thus, although the value of that parameter is difficult to measure or derive from mechanistic considerations of the glacial erosion process, we show here that it can be constrained by considering the implications of its value on the computed landform evolution, taking advantage of the dependency of ice erosion on K_g and ice velocity (and thus ice thickness, and the size of the accumulation area). Alternatively, one may consider another tectonic model (see experiment 6 and 7), which may lead to another value of K_g.

4.2.5. Experiment 6

[55] This experiment explores the influence of the rock uplift pattern on the resulting landscape. For this purpose, we use a model similar to Braun et al. (submitted manuscript, 2007), in which the maximum vertical rock uplift velocity is imposed to be located about 15 km away from the Alpine Fault (curve labeled *rB* in Figure 1). This velocity field is derived from the simple observation that the area between the main drainage divide and the Alpine Fault shows evidence of progressively enhanced deformation from undeformed rocks near the divide to ultramylonitic deformation near the Alpine Fault. All structures indicate reverse movement with thrusting of the southeastern side over the northwestern side, therefore implying an increasing rock uplift velocity from northwest to southeast. The results of this experiment are illustrated in Figure 10.

[56] After the first cycle (Figure 10b), intense erosion occurs everywhere. The regions of enhanced rock uplift near the divide are only slightly more elevated than in experiment 2. The landscape that is produced on either side of the divide is in fact very similar to the one predicted in experiment 2. After the second and third cycles (Figures 10c and 10d), the reduced rock uplift rate near the Alpine Fault makes it easier for ice erosion to compete with the tectonic rock uplift rate at the mouth of the Whataroa-Perth catchment: no internally drained basin has formed near the Alpine Fault at the end of the third cycle. In turn, large overdeepenings have formed along the west coast, similar to but deeper than those observed in experiment 3. This seems

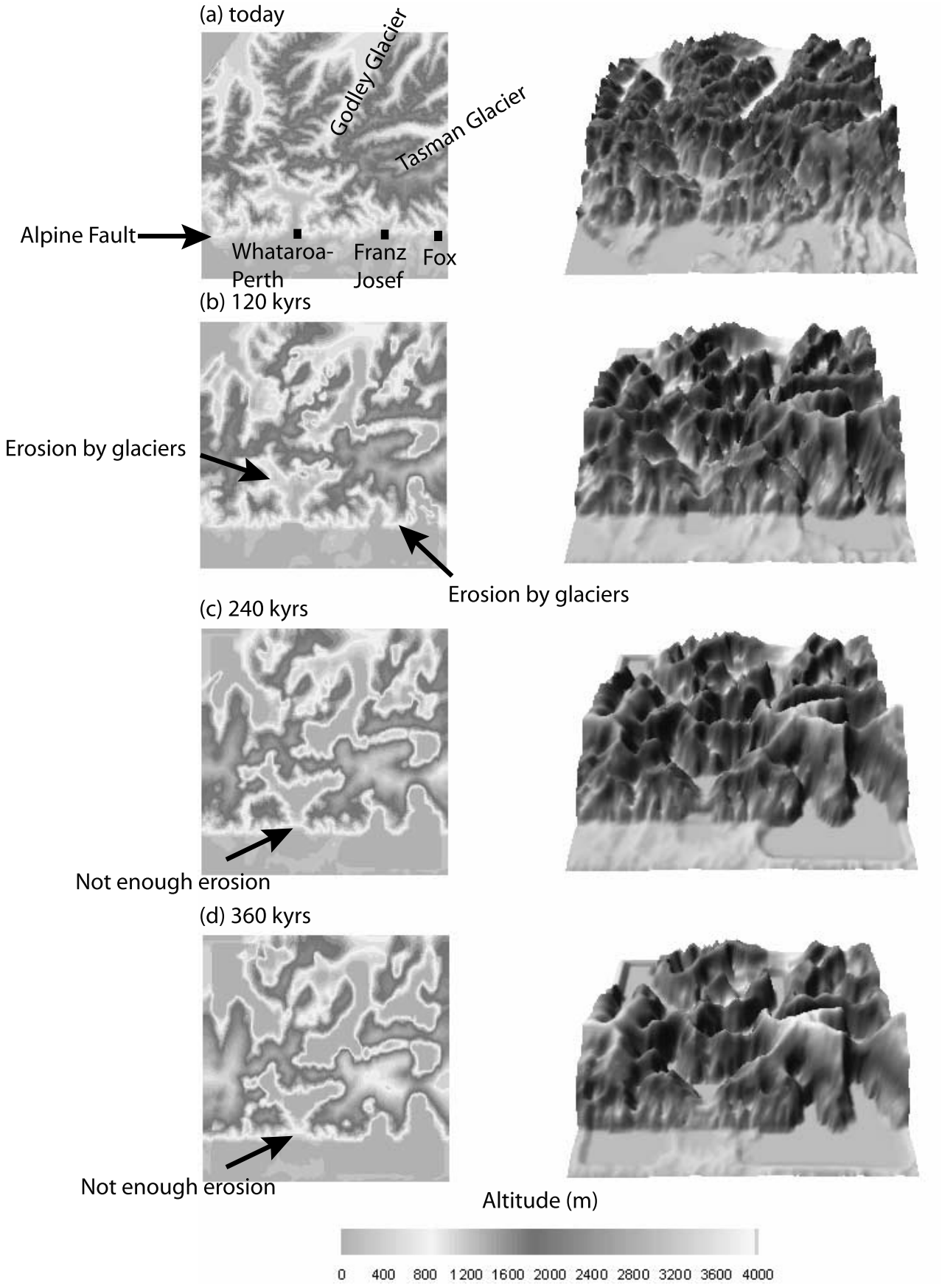

Figure 8. Experiment 4 similar to Figure 6. The value of the ice erosion constant, K_g, has been decreased with respect to experiment 2.

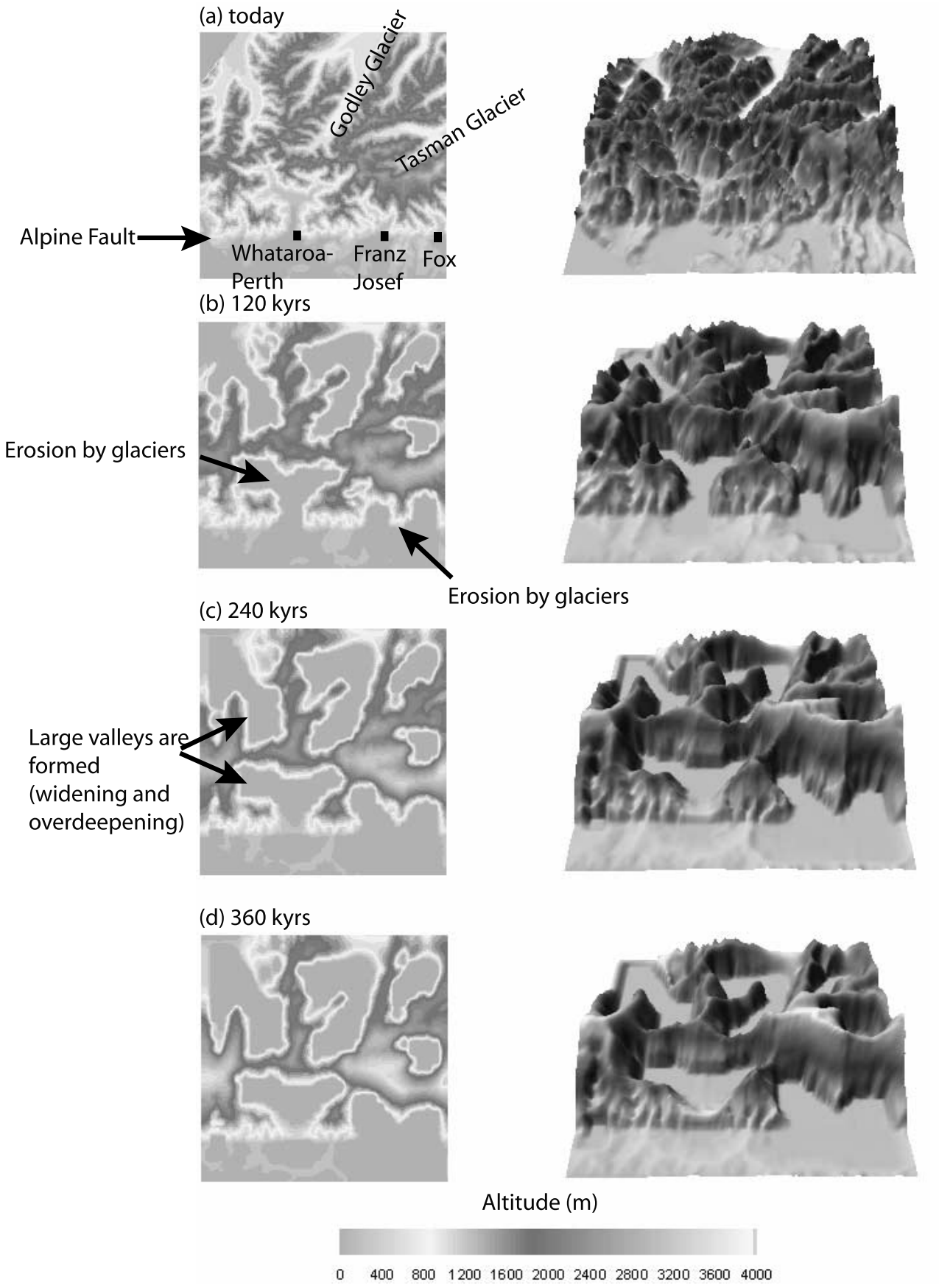

Figure 9. Experiment 5 similar to Figure 6. The value of the ice erosion constant, K_g, has been increased with respect to experiment 2.

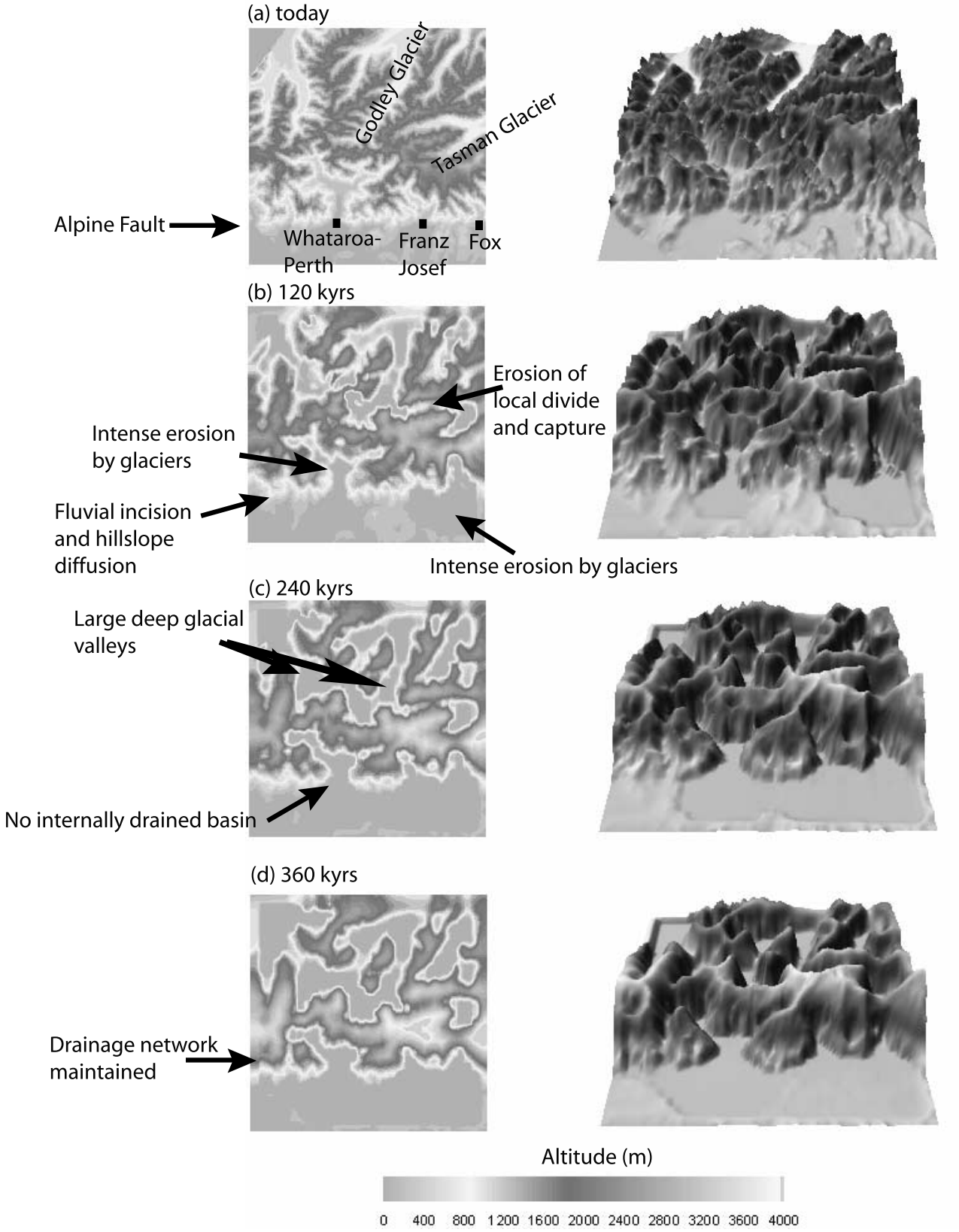

Figure 10. Experiment 6 similar to Figure 6. The maximum rock uplift rate is located near the divide.

to correlate with field observations. Indeed, several hundreds of meters of sediments have been interpreted from seismic surveys near the Alpine Fault (T. Stern personal communication, 2005). Given the set of erosional parameters, the results of this experiment appears to favor a tectonic model in which the regions of maximum rock uplift rate do not lie in the direct vicinity of the Alpine Fault.

4.2.6. Experiment 7

[57] In this final experiment, we will assume a hypothetical situation in which the climate does not oscillate with time and is forced to remain uniformly cold. This has the direct consequence that large parts of the mountain range are permanently covered with ice. In this way we wish to compare the efficiency of alternating erosion mechanisms. We use the second tectonic model (B). The results are shown in Figure 11 and should be compared to those of experiment 6 in Figure 10.

[58] In this experiment, substantial erosion occurs along the major valleys on either sides of the divide. On the southeastern side, there is no major difference with the other experiments, confirming that even under oscillating climatic conditions, erosion of that part of the landscape is dominated by glacial processes. On the northeastern side, significant enlargement and widening of the Whataroa-Perth catchment is observed. The landscape produced in this experiment exhibits a smoother topography as most of the small-scale features maintains on the low-elevation ridges by fluvial processes have disappeared. The catchment-scale relief (difference between valley floors and ridge summits) is high and greater than what is currently observed. This confirms the transitional character of the present-day landscape of the west coast of the Southern Alps described with great detail by *Herman and Braun* [2006b].

5. Discussion and Reinterpretation of Key Observations From the South Island

[59] Some key observations can be drawn from the modeling experiments. These are as follows: (1) glaciers seem to lead to complex, spatially and temporally variable erosion patterns, (2) topography may approach steady state in regions where the rock uplift rate is moderate, (3) the topography remains transient in regions of high rock uplift rate, (4) the model enable us to better describe the evolution of the topography in the Southern Alps of New Zealand, (5) the model can be used to test the kinematics of the orogen. We discuss each of these points in this section.

[60] The modeling results provide insights into the character of glacial erosion in an active orogenic system. According to model predictions, glaciers lead to very complex patterns of erosion. Figure 12 is a close-up of Figure 5f and shows the erosion patterns induced by glaciers at the glacial maximum (remembering that the color of the ice is proportional to its basal sliding velocity and thus its erosion rate). Figure 12 clearly illustrates that the geometry of the orogen and the position of the ELA, which are respectively controlled by the tectonic setting and the climate, exert the primary control on the extent of the ice cap and its subsequent erosion patterns. We see that erosion is focused on the high slope areas, either near the divide or along the steep sections of the main valleys, and where the ice accumulates by convergence of flow at the mouth of the main valleys. This leads to the formation of (1) the high-altitude, high-relief glacial landforms and (2) large overdeepenings later to be filled by glacial debris at the end of each glaciation.

[61] Because of the large variations in ice geometry during a glacial cycle, the regions of the landscape where glacial erosion is most intense vary greatly through time. Indeed, the simulations show (Figure 5) that the sliding portion of the ice cap changes position as the ice extent evolves, in turn, inducing a time-varying erosion pattern. Several factors control this evolution. Ice erosion is proportional to basal sliding, and thus the parts of the glaciers that are eroding must have a basal temperature that has reached the melting temperature. The basal temperature increases proportionally to the ice thickness, h, and surface temperature, T_s. Hence the part of the landscape where glaciers are actively eroding is a function of h and T_s. When the ice extent is maximum, basal melting occurs at lower elevations where h and T_s are relatively high; at high altitude, the ice is frozen at the ice-bedrock interface because the ice thickness is, on average, thinner (basement slopes are often higher) and T_s is lower therefore preventing the bedrock from being eroded by abrasion. Alternatively when the ice cap is less extensive, surface temperature in the elevated part of the landscape may be high enough to generate basal melting and induce some erosion. However, because the volume and thus the flow of ice is smaller, sliding velocities are smaller and erosion rates reduced.

[62] Many of the experiments led to the formation of interglacial closed, inward draining areas or lakes resulting from the formation of overdeepenings in regions of ice convergence during periods of maximum ice cover. The model is indeed strongly limited by the fact that glacial debris transport and sedimentation are not included, so that, at the end of a glacial period, there is not enough sediments to fill up these overdeepened regions. This has important consequences for the geometry of the resulting drainage patterns and the efficiency of the fluvial network during interglacial periods. Large overdeepened areas are commonly observed on real glaciated landscapes and in many parts of the South Island: examples include the large, longitudinal lakes seen on the eastern side of the divide or the overdeepened regions observed on the western side of the divide, extending for several kilometers away from the Alpine Fault. The latter are presently filled with hundreds of meters of sediments and, following the rapid current rock uplift, lead to the formation of large gravel terraces on the sides of the lower reaches of the meandering Perth and Whataroa rivers.

[63] On the southeastern side of the Main Divide, the modeling results suggest that the topography rapidly reaches some form of steady state along existing major valleys. Although glacial erosion may be very efficient during the first glacial cycle, in most experiments, there is no substantial reshaping of the landform during the following cycles. Furthermore, on that part of the landscape, the evolution of the topography is not sensitive to parameter changes (either fluvial or glacial erosion parameters) suggesting that little erosion takes place there today. These results are consistent with observations that the landscape on the southeastern side of the divide is relatively stable and mostly glacial in

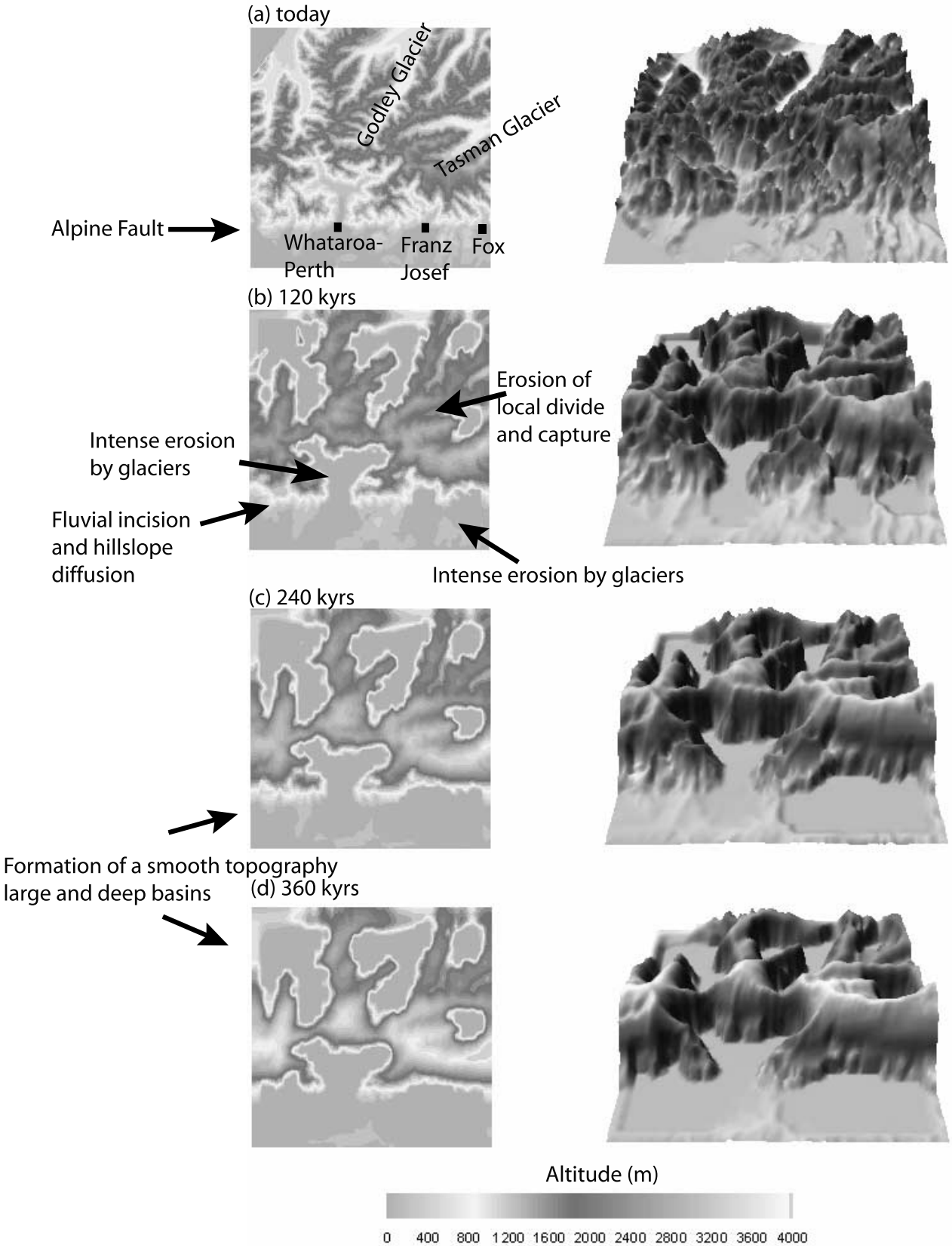

Figure 11. Experiment 7 similar to Figure 6. The climate is uniformly cold.

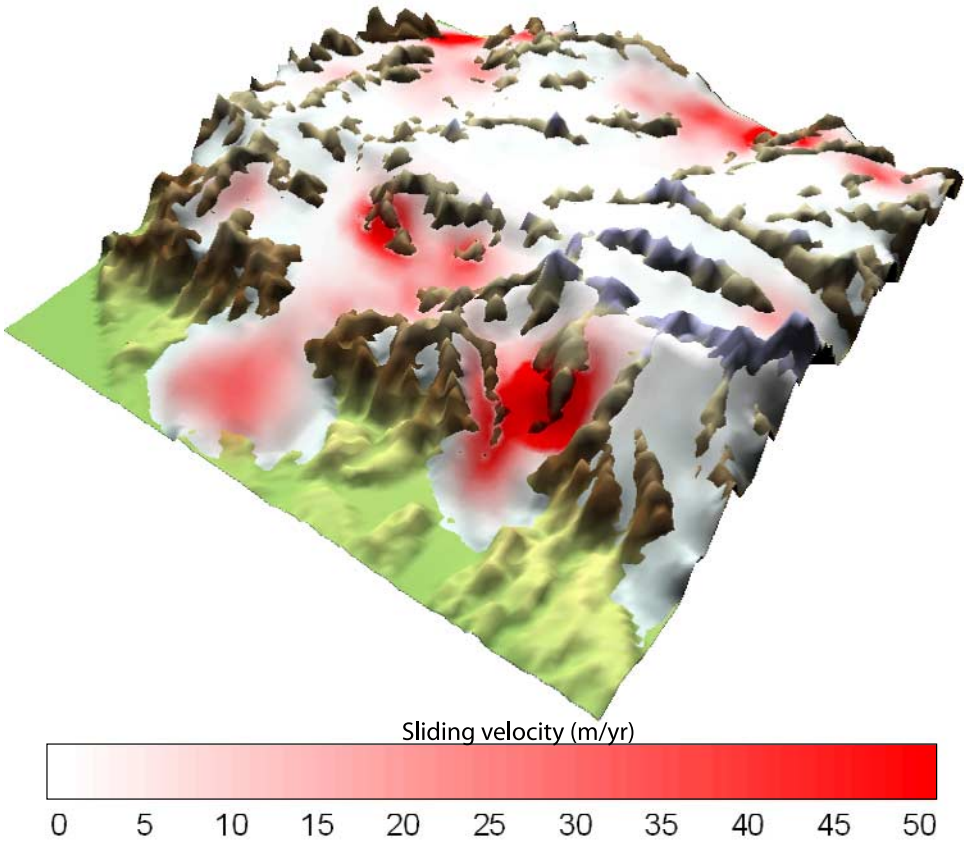

Figure 12. Close-up of Figure 5f. It illustrates the ice extent, sliding velocities, and erosion patterns at the LGM.

character. A high-resolution satellite image of the Godley Valley, one of the main valleys on the eastern side of the range, is shown in Figure 13. This wide, longitudinal valley and its upstream tributaries have all the characteristics of glacial features and have clearly been created by repeated glaciations. They are now filled with sediments on which the current river meanders. The hillslopes have preserved their glacial character (hanging valleys, cirques, erratics, etc. are very common) with little evidence of fluvial reshaping. The low tectonic rock uplift rate and the relatively low precipitation rate (compared to the extreme conditions experienced on the other side of the divide) combine here to prevent this part of the orogen to switch back to fluvially dominated erosional conditions during interglacial periods, as is the case on the western side [*Herman and Braun*, 2006b].

[64] On the western side of the range, the landscape is much more sensitive to changes in the erosion parameters. In experiment 2, the landscape rapidly reaches a steady form. However, the range of parameter values that can be used to maintain a relatively similar topography from one glacial cycle to the next is relatively narrow (e.g., change of K_f, experiment 3, or K_g, experiments 4 and 5). This demonstrates how dynamic the landscape is compared to the eastern side and how strong the potential feedback mechanisms are. These include the strong control exerted by glacial erosion on the mean elevation of the orogen, which, in turn, controls the surface area of the accumulating regions, the total volume, thickness and extent of ice and, consequently, the efficiency of glacial erosion. Locally, the climate and the geometry of the topography dictate where the different erosion processes operate, themselves leading to a modification of the topography. Ultimately, the system keeps evolving and leads to a drainage network that is very dynamic. For example, if fluvial incision and hillslope (diffusion) processes substantially modify the landform in ice-free areas during an interglacial period [*Herman and Braun*, 2006b], the glacial erosion patterns may be completely different when the ice comes back and, in turn, lead to a reorganization of the drainage network that will modify fluvial efficiency.

[65] On the timescale of a glacial cycle, these new modeling results give us a good appreciation of how the landscape evolves on the west coast of the Southern Alps. We summarize this by illustrating how a longitudinal profile (Figure 14) and its corresponding hillslopes evolve according to the qualitative observations made by *Herman and Braun* [2006b] and the quantitative results from the different numerical models presented here. In the downstream part of the longitudinal profile (i.e., near the Alpine Fault), fluvial transport is dominant during interglacial periods. The river is meandering and terraces are rock uplifted. During glacial

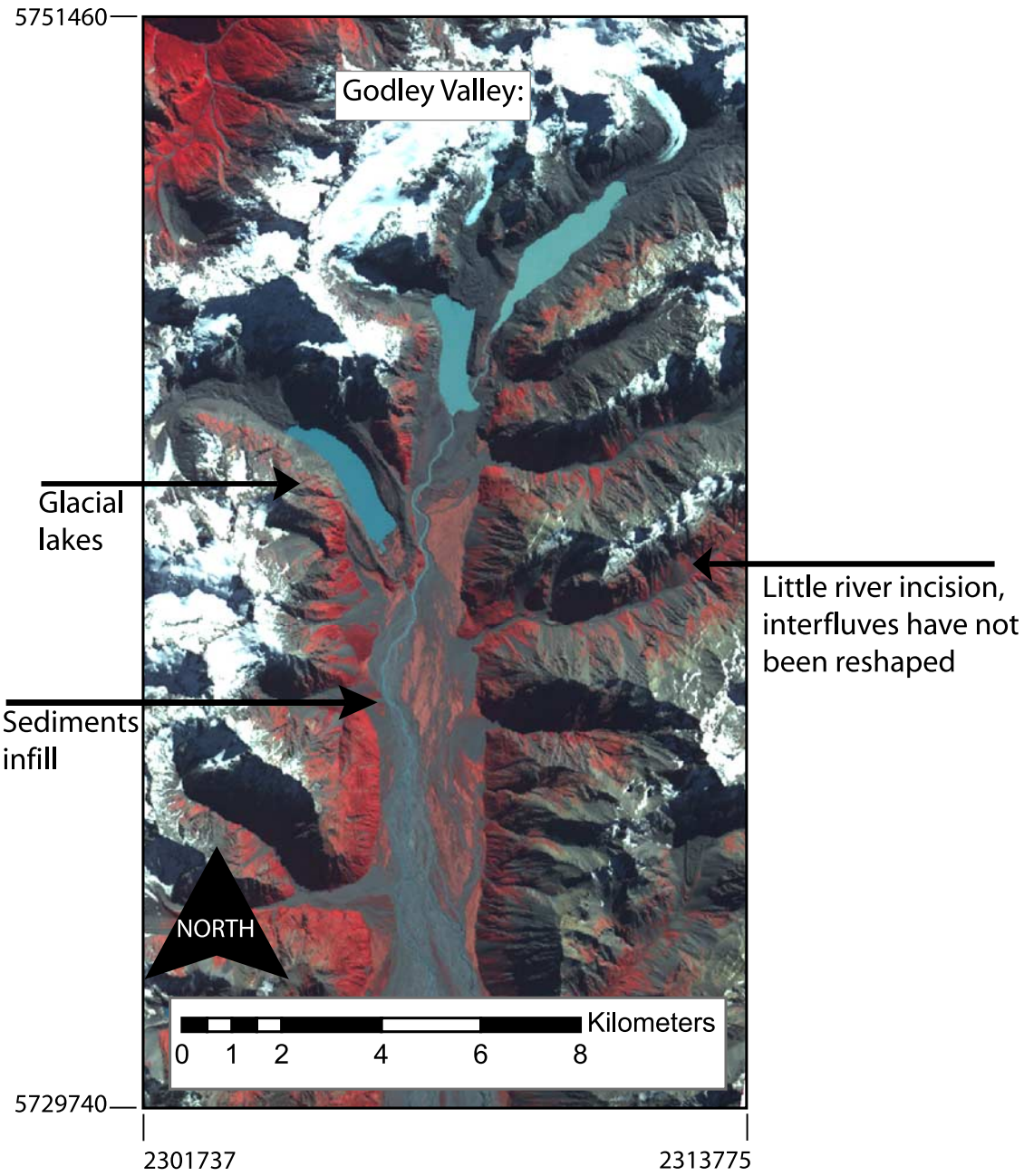

Figure 13. High-resolution satellite image (ASTER 1B) of the Godley Valley. The longitudinal valley and its upstream tributaries have the characteristics of glacial features: glacial lakes, sediments infill, hanging valleys, and glacial cirques. Note that the Godley Valley was completely filled up with ice at the LGM, as predicted by the model (Figure 4).

maxima, the large glaciers that were flowing down to sea level were very efficient and induced enough erosion to balance the rock uplift rates near the Alpine Fault and, locally, lead to the formation of substantial overdeepenings now filled by glacial deposits. In the middle part of the longitudinal profile, erosion by glaciers is important and leads to the formation of a flat longitudinal profile during glacial maxima. During glacial retreat, erosion rate decreases and the region is rapidly rock uplifted so that bedrock becomes exposed and can be incised by the river. This process propagates upward during glacial retreat. In the headwaters, the landscape remains glaciated and the profile is bounded by a glacial backwall. The evolution of the hillslopes is slightly different. Near the Alpine Fault, some parts of the landscape experience very little glacial erosion, so that fluvial incision and hillslope diffusion always dominate on the interfluves. These regions correspond to the area where numerous landslides have been mapped [*Hovius et al.*, 1997]. In the central part of the west coast, the slopes experience an erosional regime that oscillates constantly between glacial and fluvial erosion. Our modeling and the current shape of the landforms suggest that the landscape switches almost instantly (i.e., within a few thousands of years) from a glaciated to fluvially dominated

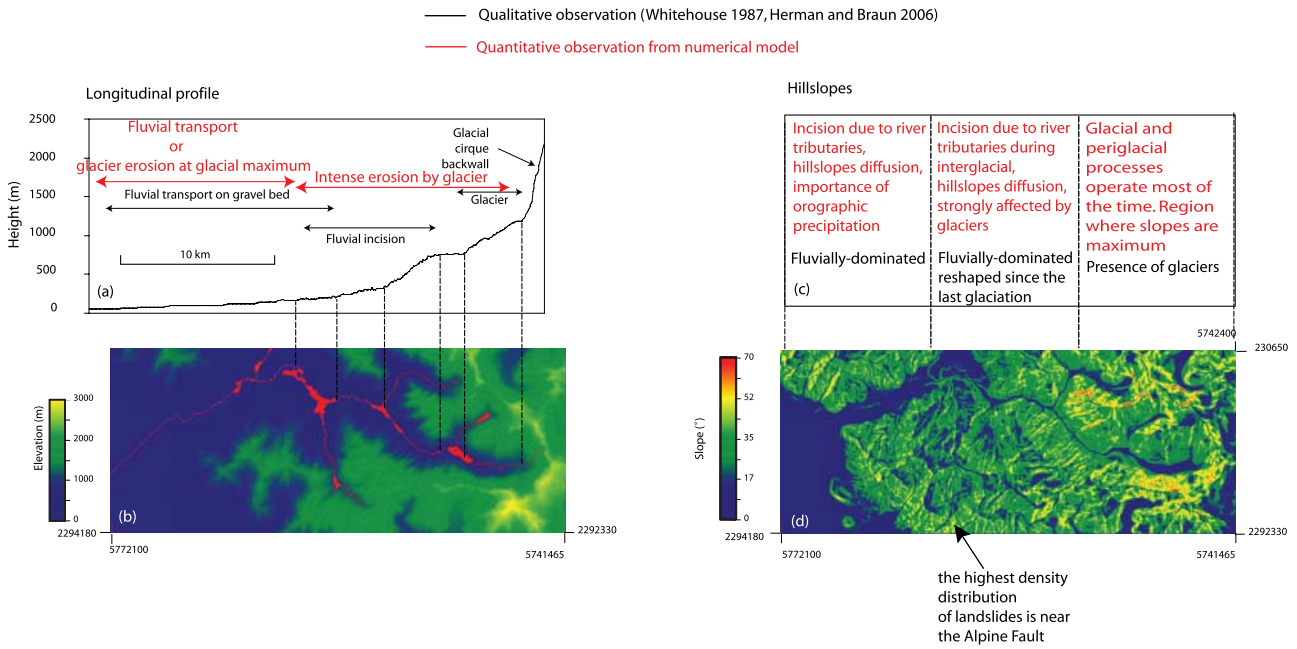

Figure 14. Evolution of the topography in the Whataroa-Perth catchment (modified from *Herman and Braun* [2006b]). (a) Longitudinal profile can be divided into three sections: (1) downstream, mainly eroded at glacial maximum; (2) central, oscillating between glacial and fluvial erosion; and (3) landscape that remains glaciated. (b) Topography. (c) Hillslopes are divided into three sections: (1) donwstream part of catchment slopes affected by fluvial incision and landsliding mostly; (2) fluvial incision, landsliding, and glacial abrasion; and (3) domination of glacial and periglacial processes. (d) Slopes. New Zealand Map grid system is used for the coordinates.

character as the ice retreats. This is highlighted by the high density of the drainage network and the occurrence of numerous landslides. In its most upstream parts, the landform remains glacially dominated most of the time as a very warm climate would be necessary to completely melt the ice in regions where the divide is high. Present-day glaciers are found nearly everywhere near the Main Divide and extend down to sea level in regions of highest topography (Mount Cook area) and thus fastest ice accumulation.

[66] The exact nature of the current rock uplift pattern in the vicinity of the Alpine Fault is poorly constrained. Recent GPS measurements [*Beavan et al.*, 2005] suggest a relatively broad rock uplift distributed over several tens of kilometers, with the location of the maximum rock uplift rate clearly offset from the surface expression of the Alpine Fault. These observations are, however, difficult to interpret in terms of the long-term tectonic rock uplift rates in part because of the effect of elastic deformation of the uppermost crust during interseismic periods. Here we have tested two end-member tectonic models. Our results seem to favor a situation in which the rock uplift rate is maximum away from the Alpine Fault. We therefore suggest that the previously accepted model in which the tectonic rock uplift is maximum directly southeast of the main thrust should be revisited.

6. Conclusions

[67] The main outcomes of this paper are as follows:

[68] 1. We have developed of a new version of an ice model similar to *Braun et al.* [1998] that can be used on a higher-resolution grid and therefore enables us to predict with greater accuracy the ice extent and its consequent erosion patterns in response to climate change. The model includes the effects of fluvial and hillslope erosion. The model is able to predict and thus explain many aspects of the present-day landform of an active mountain belt subject to strong climatic variations: the Southern Alps of New Zealand. While the model leads to very interesting results, it needs to be improved by including periglacial processes for example.

[69] 2. The model demonstrates the complexity of erosion patterns in a system affected by cyclic climatic conditions. In particular, the results show how glacial erosion patterns are clustered and evolve through a glacial cycle. They are clearly not as uniform as those resulting from fluvial erosion, although the resulting landscape may look somewhat smoother.

[70] 3. The model also explains the evolution of the wide, longitudinal valleys on the southeastern side of the Southern Alps, initially carved and now maintained by relatively slow glacial erosion. The topography seems to be near steady state and quite insensitive to a change of erosion efficiency, at the timescale of a glacial cycle.

[71] 4. Our study also favors a tectonic model in which the maximum rock uplift is offset from the Alpine Fault, closer to the divide.

[72] 5. We propose a detailed scenario for the succession of mechanisms that control the evolution of the topography on the west coast of the Southern Alps at the timescale of a glacial cycle. The major trunk is strongly affected by glaciations, down to very low altitudes. On the other hand,

hillslopes are very sensitive to climate shifts. Most of the hillslopes seem to rapidly evolve because of the high rock uplift and precipitation rates, which, in turn, renders the topography very dynamic and topographic steady state difficult to achieve in this part of the orogen.

[73] **Acknowledgments.** The authors would like to thank Alex Densmore, Todd Ehlers, and Simon Brocklehurst for their thorough and constructive reviews.

References

Adams, C. J. (1980), Contemporary uplift rates and erosion of the Southern Alps, New Zealand, *Geol. Soc. Am. Bull.*, *91*, 1–114.

Alley, R., D. Lawson, G. Larson, E. Evenson, and G. Baker (2003), Stabilizing feedbacks in glacier-bed erosion, *Nature*, *424*, 758–760.

Anderson, R., P. Molnar, and M. Kessler (2006), Features of glacial valley profiles simply explained, *J. Geophys. Res.*, *111*, F01004, doi:10.1029/2005JF000344.

Andrews, J. (1972), Glacier power, mass balances, velocities and erosional potential, *Z. Geomorphol.*, *13*, 1–17.

Avouac, J.-P., and E. Burov (1996), Erosion as a driving mechanism of intracontinental mountain growth, *J. Geophys. Res.*, *101*, 17,747–17,769.

Barrows, T. T., S. Juggins, P. DeDeckker, J. Thiede, and J. Martinez (2000), Sea-surface temperatures of the southwest Pacific Ocean during the Last Glacial Maximum, *Paleoceanography*, *15*, 95–109.

Batt, G. E., and J. Braun (1999), The tectonic evolution of the Southern Alps, New Zealand: Insights from fully thermally coupled dynamical modelling, *Geophys. J. Int.*, *136*, 403–420.

Beaumont, C., P. Fullsack, J. Hamilton (1992), Erosional control of active compressional orogens, in *Thrust Tectonics*, edited by K. R. McClay, pp. 1–18, Chapman and Hall, New York.

Beavan, J., D. Matheson, P. Denys, M. Denham, T. Herring, B. Hager, M. P. Molnar (2005), A vertical deformation profile across the Southern Alps, New Zealand, from 3.5 years of continuous GPS data, in *Proceedings of the Workshop: The State of GPS Vertical Positioning Precision: Separation of Earth Processes by Space Geodesy*, *Cah. Cent. Eur. Geodyn. Seismol.*, vol. 23, edited by T. Van Dam and O. Francis, pp. 111–123, Cent. Eur. de Geodyn. et Seismol., Luxembourg.

Boulton, G. (1974), Process and patterns of glacial erosion, in *Glacial Geomorphology*, edited by D. R. Coates, pp. 41–87, State Univ. of N.Y. at Binghamton, Binghamton.

Boulton, G. (1979), Processes of glacier erosion on different substrata, *J. Glaciol.*, *23*, 15–38.

Braun, J., and M. Sambridge (1997), Modelling landscape evolution on geological time scales: A new method based on irregular spatial discretization, *Basin Res.*, *9*, 27–52.

Braun, J., G. E. Batt, D. L. Scott, H. McQueen, and A. R. Beasley (1994), A simple kinematic model for crustal deformation along two- and three-dimensional listric normal faults derived from scaled laboratory experiments, *J. Struct. Geol.*, *16*, 1477–1490.

Braun, J., D. Zwartz, and J. Tomkin (1998), A new surface-processes model combining glacial and fluvial erosion, *Ann. Glaciol.*, *28*, 282–290.

Brocklehurst, S. H., and K. X. Whipple (2002), Glacial erosion and relief production in the eastern Sierra Nevada, *Geomorphology*, *42*, 1–24.

Brozovic, N., D. W. Burbank, and A. J. Meigs (1997), Climatic limits on landscape development in the northwestern Himalayas, *Science*, *276*, 571–574.

Burbank, D. W., A. E. Blythe, J. Putkonen, B. Pratt-Sitaula, E. Gabet, M. Oskin, A. Barros, and T. Ojha (2003), Decoupling of erosion and precipitation in the Himalayas, *Nature*, *426*, 652–655.

Chamberlain, C., M. Poage, D. Craw, and R. Reynolds (1999), Topographic development of the Southern Alps recorded by the isotopic composition of authigenic clay minerals, South Island, New Zealand, *Chem. Geol.*, *155*, 279–294.

Chinn, T. J. H. (1995), Glacier fluctuations in the Southern Alps of New Zealand determined from snowline elevations, *Arct. Alp. Res.*, *27*, 187–197.

Davis, W. M. (1892), The convex profile of badland divides, *Science*, *20*, 245.

Densmore, M., T. A. Ehlers, and G. Woodsworth (2007), Effect of alpine glaciation on thermochronometer age-elevation profiles, *Geophys. Res. Lett.*, *34*, L02502, doi:10.1029/2006GL028371.

Dulla, W. (1991), Geometric models of listric normal faults and rollover folds, *AAPG Bull.*, *75*, 1609–1625.

Ehlers, T. A., K. A. Farley, M. Rusmore, and G. Woodsworth (2006), Apatite (U-Th)/He signal of large magnitude accelerated glacial erosion, southwest British Columbia, *Geology*, *34*, 765–768.

EPICA community members (2004), Eight glacial cycles from an Antarctic ice core, *Nature*, 429, 623–628.

Fabel, D., J. M. Harbor, D. Dahms, A. James, D. Elmore, L. Horn, K. Daley, and C. Steele (2004), Spatial patterns of glacial erosion at a valley scale derived from terrestrial cosmogenic ^{10}Be and ^{26}Al concentrations in rock, *Ann. Assoc. Am. Geogr.*, *94*(2), 241–255.

Fitzharris, B. B., T. J. H. Chinn, and G. N. Lamont (1997), Glacier balance fluctuations and atmospheric circulation patterns over the Southern Alps, New Zealand, *Int. J. Climatol.*, *17*, 1–19.

Gage, M., and R. Suggate (1958), Glacial chronology of the New Zealand Pleistocene, *Am. Geol. Soc. Bull.*, *69*, 575–588.

Gilbert, G. K. (1909), The convexity of hilltops, *J. Geol.*, *17*, 344–350.

Hallet, B. (1979), A theoretical model of glacial abrasion, *J. Glaciol.*, *17*, 209–222.

Hallet, B. (1996), Glacial quarrying: A simple theoretical model, *Ann. Glaciol.*, *22*, 1–8.

Harbor, J. (1992a), Application of a general sliding law to simulating flow in a glacier cross section, *J. Glaciol.*, *38*, 182–190.

Harbor, J. (1992b), Numerical modelling of the development of u-shaped valleys by glacial erosion, *Geol. Soc. Am. Bull.*, *104*, 1364–1375.

Herman, F., J. Braun. (2006a), A parametric study of soil transport mechanisms, in *Tectonics, Climate, and Landscape Evolution*, edited by S. Willett et al., *Geol. Soc. Am. Spec. Pap.*, 398, 191–200, doi:10.1130/2006.2398(11).

Herman, F., and J. Braun (2006b), Fluvial response to horizontal shortening and glaciations: A study in the Southern Alps of New Zealand, *J. Geophys. Res.*, *111*, F01008, doi:10.1029/2004JF000248.

Herman, F., J. Braun, and W. Dunlap (2007), Tectonomorphic scenarios in the Southern Alps of New Zealand, *J. Geophys. Res.*, *112*, B04201, doi:10.1029/2004JB003472.

Hindmarsh, R., and A. Payne (1996), Time-step limit for stable solutions of the ice-sheet equation, *Ann. Glaciol.*, *23*, 74–85.

Hooke, R. L. (1998), *Principles of Glacier Mechanics*, Prentice-Hall, Upper Saddle River, N.J.

Hovius, N., C. P. Stark, and P. A. Allen (1997), Sediment flux from a mountain belt derived from landslide mapping, *Geology*, *25*, 231–234.

Howard, A. D. (1994), A detachment-limited model of drainage basin evolution, *Water Resour. Res.*, *30*, 2261–2285.

Hutter, K. (1983), *Theoretical Glaciology*, Reidel, D. Dordrecht, Netherlands.

Johnston, P. (1993), The effect of spatially nonuniform water loads on prediction of sea-level change, *Geophys. J. Int.*, *14*, 615–634.

Kaab, A. (2002), Monitoring high-mountain terrain deformation from repeated air- and spaceborne optical data: Examples using digital aerial imagery and ASTER data, *ISPRS J. Photogramm. Remote Sens.*, *57*(1-2), 39–52.

Kamp, P., and J. Tippett (1993), Dynamics of the Pacific Plate crust in the South Island (New Zealand) zone of oblique continent-continent convergence, *J. Geophys. Res.*, *98*, 16,105–16,118.

Kessler, M., and R. Anderson (2004), Testing a numerical glacial hydrological model using speed-up events and outburst floods, *Geophys. Res. Lett.*, *31*, L18503, doi:10.1029/2004GL020622.

Kessler, M., R. Anderson, and G. Stock (2006), Modeling topographic and climatic control of east-west asymmetry in Sierra Nevada glacier length during the Last Glacial Maximum, *J. Geophys. Res.*, *111*, F02002, doi:10.1029/2005JF000365.

Knap, W., J. Oerlemans, and M. Cadee (1996), Climate sensitivity of the ice cap of King George Island, South Shetlands, Antarctica, *Ann. Glaciol.*, *23*, 154–159.

Koons, P. O. (1987), Thermal and mechanical consequences of rapid uplift in continental collision; An example from the Southern Alps, New Zealand, *Am. J. Sci.*, *289*, 1041–1069.

Koons, P. O. (1990), Two-sided orogen: Collision and erosion from the sandbox to the Southern Alps, New Zealand, *Geology*, *18*, 679–682.

Koppes, M., and B. Hallet (2006), Erosion rates during rapid deglaciation in Icy Bay, Alaska, *J. Geophys. Res.*, *111*, F02023, doi:10.1029/2005JF000349.

Lambeck, K., T. Esat, and E.-K. Potter (2002), Links between climate and sea levels for the past three million years, *Nature*, *419*, 199–206.

Levitius, S., and T. Boyer (1994), *World Ocean Atlas 1994*, vol. 4, *Temperature, NOAA Atlas NESDIS 4*, 129 pp., Nat. Oceanic and Atmos. Admin., Silver Spring, Md.

Little, T. A., and R. J. Holcombe (2002), Kinematics of oblique collision and ramping inferred from microstructures and strain in middle crustal rocks, central Southern Alps, New Zealand, *J. Struct. Geol.*, *24*, 219–239.

Little, T. A., S. Cox, J. Vry, and G. Batt (2005), Variations in exhumation level and uplift rate along the oblique-slip Alpine fault, central Southern Alps, New Zealand, *Geol. Soc. Am. Bull.*, *117*, 707–723, doi:10.1130/B25500.

Lliboutry, L. (1994), Monolithologic erosion of hard beds by temperate glaciers, *J. Glaciol.*, *40*, 433–450.

MacGregor, K., R. S. Anderson, S. Anderson, and E. Waddington (2000), Numerical simulations of glacial longitudinal profile evolution, *Geology*, *28*, 1031–1034.

Molnar, P., and P. England (1990), Late Cenozoic uplift of mountain ranges and global climate change: Chicken and egg?, *Nature*, *346*, 29–34.

Nelson, C., P. Cooke, C. Hendy, and G. Cuthberston (1993), Oceanographic and climatic changes over the past 160,000 years at Deep Sea Drilling Project site 594 off southeastern New Zealand, southwest Pacific Ocean, *Paleoceanography*, *8*, 435–458.

Norris, R. J., and A. F. Cooper (2000), Late Quaternary slip rates and slip partitioning on the alpine fault, New Zealand, *J. Struct. Geo.*, *23*, 507–520.

Nunn, J., and J. Aires (1988), Gravity anomalies and flexure of the lithosphere at the Middle Amazon Basin, Brazil, *J. Geophys. Res.*, *93*, 415–428.

Paterson, W. (1994), *The Physics of Glaciers*, 3rd ed., Elsevier, New York.

Pattyn, F. (2003), A new three-dimensional higher-order thermomechanical ice sheet model: Basic sensitivity, ice stream development, and ice flow across subglacial lakes, *J. Geophys. Res.*, *108*(B8), 2382, doi:10.1029/2002JB002329.

Petit, J., et al. (1999), Climate and atmospheric history of the past 420000 years from the Vostok ice core, Antarctica, *Nature*, *399*, 429–436.

Porter, S. C. (1975), Equilibrium-line altitudes of the late Quaternary glaciers in the Southern Alps, New Zealand, *Quat. Res.*, *5*, 27–47.

Raymo, M. E., and W. F. Ruddiman (1992), Tectonic forcing of the late Cenozoic climate, *Nature*, *359*, 117–122.

Reiners, P. W., T. A. Ehlers, S. G. Mitchell, and D. R. Montgomery (2003), Coupled spatial variations in precipitation and long-term erosion rates across the Washington Cascades, *Nature*, *426*, 645–647.

Sambridge, M. (1999), Geophysical inversion with a neighbourhood algorithm—I. Searching a parameter space, *Geophys. J. Int.*, *138*, 479–494.

Shuster, D. L., T. A. Ehlers, M. E. Rusmoren, and K. A. Farley (2005), Rapid glacial erosion at 1.8 Ma revealed by $^{4}He/^{3}He$ thermochronometry, *Science*, *310*, 1668–1670.

Soons, J. M. (1979), Late Quaternary environments in the central South Island of New Zealand, *N. Z. Geogr.*, *35*, 16–23.

Spotila, J. A., J. T. Busher, A. J. Meigs, and P. W. Reiners (2004), Long-term glacial erosion of active mountain belts: Example of the Chugach–St. Elias Range, Alaska, *Geology*, *32*, 501–504.

Stern, T. A. (1995), Gravity anomalies and crustal loading at and adjacent to the Alpine Fault, New Zealand, *N. Z. J. Geol. Geophys.*, *38*, 593–600.

Suggate, R. P. (1990), Late Pliocene and Quaternary glaciations of New Zealand, *Quat. Sci. Rev.*, *9*, 175–197.

Suggate, R. P., and P. Almond (2005), Last Glacial Maximum (LGM) in western South Island, New Zealand: Implications for the global LGM and MIS2, *Quat. Sci. Rev.*, *24*, 1923–1940.

Svennson, H. (1958), Is the cross-section of a glacial valley a parabola?, *J. Glaciol.*, *3*, 362–363.

Tippett, J. M., and P. J. J. Kamp (1993), Fission track analysis of the late Cenozoic vertical kinematics of continental Pacific Crust, South Island, New Zealand, *J. Geophys. Res.*, *98*, 16,119–16,148.

Tomkin, J. (2000), Landforming processes in glaciated orogens: A numerical study, Ph.D. thesis, Aust. Natl. Univ., Canberra, ACT.

Tomkin, J. H., and J. Braun (2002), The effect glaciation has on the relief of a fast growing orogen: A numerical modelling study, *Am. J. Sci.*, *302*, 169–190.

Turcotte, D. L., G. Schubert (1982), *Geodynamics: Applications of Continuum Physics to Geological Problems*, 1st ed., John Wiley, New York.

Verral, P. (1981), *Joint Association for Petroleum Exploration Course Notes Number 7: Structural Interpretation With Application to North Sea Problems*, Geol. Soc., London.

Walcott, R. I. (1998), Present tectonics and late Cenozoic evolution of New Zealand, *Rev. Geophys.*, *36*, 1–26.

Whipple, K. X., and G. E. Tucker (1999), Dynamics of the stream-power river incision model: Implications for height limits of mountain ranges, landscape response timescales, and research needs, *J. Geophys. Res.*, *104*, 17,661–17,674.

Whipple, K. X., E. Kirby, and S. H. Brocklehurst (1999), Geomorphic limits to climate-induced increases in topographic relief, *Nature*, *401*, 39–43.

White, N., J. Jackson, and D. P. McKenzie (1986), The relationship between the geometry of normal faults and that of the sedimentary layers in their hanging walls, *J. Struct. Geol.*, *8*, 897–909.

Whitehouse, I. E. (1987), Geomorphology of a compressional plate boundary: Southern Alps, New Zealand, in *Proceedings of the First International Conference on Geomorphology—Part 1*, pp. 897–924, John Wiley, Chichester, UK.

Willett, S., C. Beaumont, and P. Fullsack (1993), Mechanical model for the tectonics of doubly-vergent compressional orogens, *Geology*, *21*, 371–374.

Willett, S. D. (1999), Orogeny and orography: The effects of erosion on the structure of mountain belts, *J. Geophys. Res.*, *104*, 28,957–28,981.

Willett, S. D., R. Slingerland, and N. Hovius (2001), Uplift, shortening, and steady state topography in active mountain belts, *Am. J. Sci.*, *301*, 455–485.

Williams, G., and I. Vann (1987), The geometry of listric normal faults and deformation in their hanging-walls, *J. Struct. Geol.*, *9*, 789–795.

J. Braun, Géosciences Rennes, Université de Rennes 1, F-35042 Rennes Cedex, France.

F. Herman, Geologisches Institut, ETH Zurich, Haldenbachstrasse 44, CH-8092, Zurich, Switzerland. (frederic@erdw.ethz.ch)